FABRY-PEROT OBSERVATIONS AND NEW MODELS OF THE HH 47A AND HH 47D BOW SHOCKS

JON A. MORSE,[1,2] PATRICK HARTIGAN,[3] STEVE HEATHCOTE,[4] JOHN C. RAYMOND,[5] AND GERALD CECIL[6]

ABSTRACT

We present new models for the HH 47A and HH 47D bow shocks based on line flux and velocity maps obtained with an imaging Fabry-Perot spectrometer. We confirm that HH 47A and HH 47D each show a bow shock/Mach disk morphology, and that velocity variability in the outflow can account for the observed structures. While it was suggested a decade ago that the inner working surface HH 47A appears to be traveling into the wake of HH 47D, we find kinematic evidence that the outer bow shock HH 47D is also not the primary ejection event in the outflow but follows in the wake of previously ejected material. By comparing the observed line ratios and line profiles to those predicted by our bow shock models, we find that both bow shocks have substantially lower shock velocities than their space motions would imply, and that the emission from each bow shock is systematically blueshifted from the rest-frame velocity of the ambient emission, indicating a comoving preshock medium. We derive kinematic ages of ~ 1150 yr for HH 47D and ~ 550 yr for HH 47A, which implies that the stellar driving source may undergo repetitive eruptions similar to FU Orionis–type outbursts every several hundred years. This timescale is similar to estimates made by Reipurth and collaborators for the separation between major outbursts in the HH 34 and HH 111 stellar jets.

Subject headings: ISM: jets and outflows — shock waves — stars: individual (HH 47A, HH 47D) — stars: pre–main-sequence

1. INTRODUCTION

High-velocity bipolar outflows may play an important role in the formation of stars by transporting angular momentum gained during the accretion of circumstellar matter away from the protostar. They may also be responsible for dispersing much of the circumstellar envelope from which the new star formed. The outflows are visible optically as highly collimated, fast jets that often are surrounded by a less collimated, slower molecular flow. There is some suggestion that the fast stellar jet may drive a molecular outflow, but this is presently uncertain. A popular scenario for generating the high-velocity bipolar outflows is that a strong magnetic field embedded in a circumstellar disk taps the gravitational energy released during accretion and accelerates and focuses material along an axis perpendicular to the accretion disk (e.g., see Pudritz, Pelletier, & Gomez de Castro 1991; Wardle & Königl 1993). This ejection mechanism implies that the evolution of the accretion disk and the stellar jet are coupled, so detailed observations of the dynamics of stellar jets may tell us about the time history of accretion at the stellar source as well as the nature of the circumstellar medium.

Multiple bow shocks that accelerate and excite ambient gas ahead of the ejected material have recently been identified along several stellar jets (e.g., in HH 34, Reipurth & Heathcote 1992; in HH 111, Reipurth, Raga, & Heathcote 1992), suggesting that the outflows, and, hence, the accretion rates, are nonsteady. In this paper we present Fabry-Perot observations and new models of the two major bow shocks along the blueshifted lobe of the HH 46/47 stellar jet. Emission from the associated Mach disks interior to each bow shock where the jet material is slowed is also detected. (A bow shock–Mach disk combination is known as a "working surface;" e.g., see Hartigan 1989.) The HH 46/47 outflow was the first of the well-studied optical jets where the presence of multiple shock structures along the same lobe of the outflow implicated possible episodic ejections from the stellar source, perhaps related to FU Orionis–type eruptions (Dopita 1978).

The HH 46/47 system was discovered by Schwartz (1977) in the dense Bok globule 210-6A (Hartley et al. 1986) at the edge of the Gum nebula and is among the brightest and best studied of the optical bipolar outflows that emanate from young stars. In the discovery paper, it was suggested that the expansion of the Gum nebula (possibly an ancient supernova remnant) has compressed the globule and triggered the star formation event responsible for the HH 46/47 outflow. The driving star has been detected in the far-IR by Emerson et al. (1984) and at 2.2 μm by Graham & Heyer (1989), with a luminosity $L_* \sim 15\,L_\odot$. It excites a bright, highly variable reflection nebula (Graham 1987) at the base of a complicated blueshifted filament, with major features labeled HH 46 and HH 47B, that protudes from the parent globule and terminates at the working surface HH 47A (see Fig. 1). Beyond HH 47A is the faint blueshifted bow shock HH 47D. On the opposite side of the source lies the redshifted bow shock HH 47C (not shown in Fig. 1), at about the same projected distance from the source as HH 47D.

Dopita (1978) and Dopita, Binette, & Schwartz (1982a) first presented low-resolution spectra of HH 46/47, and discussed their low-excitation nature in terms of radiative shock waves.
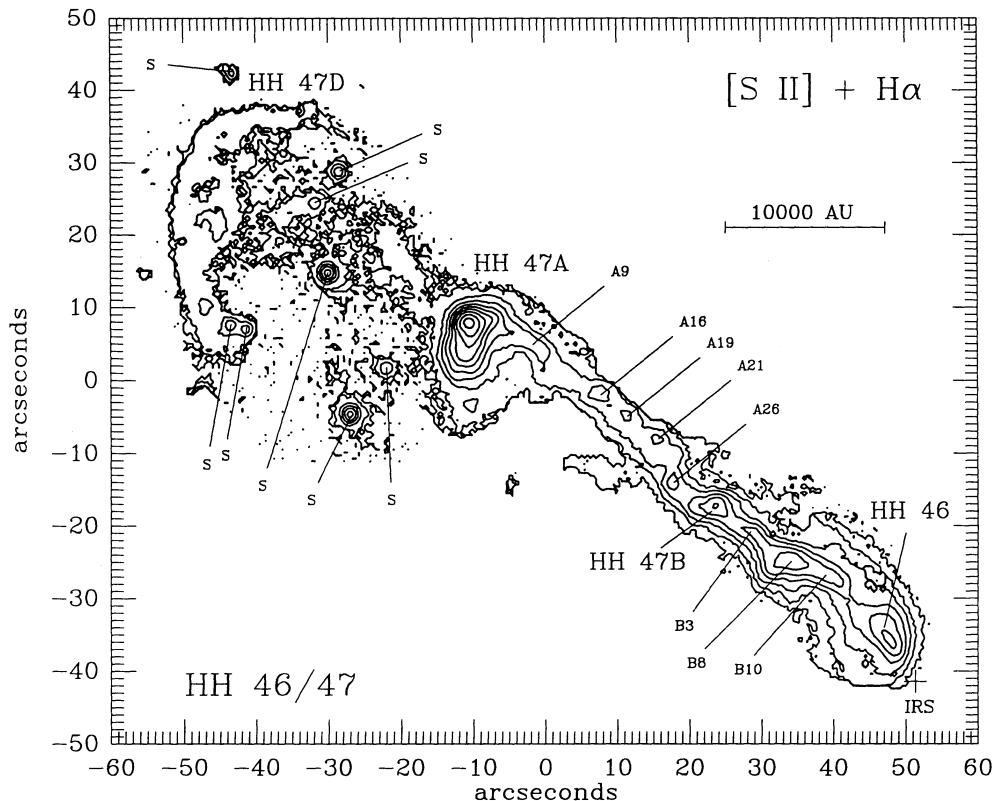
[1] Visiting Astronomer, Cerro Tololo Inter-American Observatory, operated by the National Optical Astronomy Observatories under contract to the National Science Foundation.

[2] Space Telescope Science Institute, 3700 San Martin Drive, Baltimore, MD 21218. Also Department of Physics and Astronomy, University of North Carolina, Chapel Hill.

[3] Five College Astronomy Department, Graduate Research Tower B, 517G, University of Massachusetts, Amherst, MA 01003.

[4] Cerro Tololo Inter-American Observatory, Casilla 603, La Serena, Chile 1353.

[5] Harvard-Smithsonian Center for Astrophysics, 60 Garden Street, Cambridge, MA 02138.

[6] Department of Physics and Astronomy, University of North Carolina, CB 3255 Phillips Hall, Chapel Hill, NC 27599-3255.

738

FIG. 1.—Logarithmic contour diagram of the combined Hα and [S II] λλ6716, 6731 emission showing the main features in the blueshifted lobe of the HH 46/47 system. North is to the top, and east is to the left. The labeled features follow the designation of RH91. The stellar energy source has been detected in the infrared and is marked just below and to the right of HH 46 at the edge of the optical emission. The scale bar shown assumes a distance of 450 pc to HH 46/47. Objects labeled S are stars.

Dopita, Schwartz, & Evans (1982b) and Graham & Elias (1983) obtained moderate-dispersion spectra and found radial velocities in HH 46 and HH 47A to be blueshifted within a heliocentric velocity range of ~ -100 to -170 km s^{-1}, while HH 47C was redshifted at $\sim +100$ km s^{-1}. These data were combined with the proper-motion measurements of Schwartz, Jones, & Sirk (1984) to establish the bipolar nature of the outflow. Subsequent high-resolution long-slit spectra by Meaburn & Dyson (1987) detailed the kinematics of the HH 47 jets. Raga & Mateo (1987) used narrow-band emission-line images of HH 47A and the HH 47 jet to show that the electron densities in HH 47A were much higher and the gaseous excitation much lower than along the jet, contary to the situation in many other HH jets (e.g., HH 34, HH 111; see Bührke, Mundt, & Ray 1988, Reipurth et al. 1992, Morse et al. 1993b).

The HH 46/47 system has an associated CO outflow that has been mapped by Chernin & Masson (1991) and by Olberg, Reipurth, & Booth (1992). They found that the CO emission is bipolar, but that the redshifted lobe, into the cloud, is more extensive and massive. Chernin & Masson (1991) interpreted the CO emission as arising in ambient gas that has been entrained by the high-velocity jet, and that the weak blue-shifted lobe results from a lack of entrainable molecular gas as the flow breaks out of the host globule.

Two recent studies by Hartigan, Raymond, & Meaburn (1990, hereafter HRM90) and Reipurth & Heathcote (1991, hereafter RH91) have revealed much about the detailed structure of the HH 46/47 system. The results presented here com-

plement the analyses presented in these two studies. HRM90 presented narrow-band emission-line images of the system, including a striking [O II] image which showed that the wings of the outer bow shock HH 47D extend all the way back to the HH 46 reflection nebula. They also presented echelle spectrograms in Hα that revealed distinct "hook-shaped" position-velocity profiles for HH 47A and HH 47D that are characteristic of spatially resolved bow shocks. Using the bow shock geometry described in Hartigan, Raymond, & Hartmann (1987, hereafter HRH87), they presented theoretical position-velocity diagrams for HH 47D and HH 47A. Based on the systematic blueshift observed in the position-velocity diagram, they argued that HH 47A is a bow shock moving into a preshock medium that already has a large outward velocity, i.e., a separate ejection moving into the wake of HH 47D. This provided kinematic evidence for the suggestion by Dopita et al. (1982a) that the presence of multiple bow shocks can be explained with a variable or pulsed jet. HRM90 also identified a [S II] bright knot several arcseconds behind the leading edge of the HH 47D bow shock as the Mach disk in the working surface, where the impinging jet material is slowed.

RH91 presented narrow-band emission-line images in [S II] and Hα obtained in $\sim 0\rlap{.}''7$ FWHM seeing on the ESO 3.5 m New Technology Telescope. These high-resolution images first showed that the jet appears to split into two strands between HH 47B and HH 47A. Based on the present Fabry-Perot observations, we have argued elsewhere (Hartigan et al. 1993) that the apparent splitting of the jet shows the velocity and

excitation characteristics consistent with the high-velocity stellar jet entraining the surrounding material. RH91 also resolved the photocenter at the apex of HH 47A into two distinct components, a slightly elongated leading knot and a broad, planar-looking trailing component. They subtracted the Hα image from the [S II] image to show that the leading component, along with most of the wings, was bright in [S II]. However, the trailing component was found to be brighter in Hα. Based on this difference in excitation, they concluded that the two components represent the bow shock and Mach disk in HH 47A.

We are surveying several of the most prominent stellar jet systems with an imaging Fabry-Perot spectrometer which allows us to obtain emission-line images at small velocity intervals. In previous papers (Morse et al. 1992, 1993a) we have investigated the velocity fields, electron densities and excitation conditions of the bow shocks and Mach disks at the heads of the HH 34 and HH 111 jets. This paper presents our analysis of the most prominent working surfaces in the blueshifted lobe of the HH 46/47 jet. In § 2 we summarize our observations and data reductions. Our results appear in § 3. In §§ 4 and 5 we analyze the Fabry-Perot data of HH 47D and HH 47A and present new models for the bow shock emission from each region.

2. OBSERVATIONS AND REDUCTIONS

We observed the HH 46/47 stellar jet using the Rutgers/CTIO CCD-based imaging Fabry-Perot on the CTIO 4 m telescope in 1991 February and 1992 January in $\sim 1''3$ FWHM seeing. We obtained full spatial and partial kinematic sampling of the blueshifted lobe in the Hα and [S II] $\lambda\lambda6716, 6731$ emission lines, using the "narrow" etalon which had a free spectral range of 18 Å and FWHM resolution of 0.7 Å. The CCD detector provided an image scale of $\sim 0''4$ pixel^{-1} and a field of diameter $\sim 2''5$. Narrow-band filters were placed in the collimated beam in front of the etalon in order to pass ~ 1 spectral order. The central wavelengths (FWHM bandpasses) for the Hα and [S II] filters were 6563 Å (12 Å), 6718 Å (22 Å) and 6732 Å (22 Å), respectively. Exposures were 720 s for the Hα images and 600 s for the [S II] images. We discussed the kinematics and excitation conditions in the HH 47 jet based on these observations in Hartigan et al. (1993); here we focus on the HH 47D and HH 47A working surfaces.

All of our CCD images were bias-subtracted, corrected for atmospheric extinction, and spatially registered using standard IRAF routines. The spectrophotometric standard star LTT 4364 was observed to convert CCD counts to absolute fluxes. We used our standard Fabry-Perot flat fielding, ambient ring subtraction and phase correction techniques, as described in Morse et al. (1992, 1993a), to process the data. The phase corrected data cubes consist of 17 velocity slices in Hα spanning a total heliocentric velocity range from -210 km s^{-1} to $+30$ km s^{-1}, sampled at 15 km s^{-1} intervals, and 10 velocity slices in each line of the [S II] doublet from -210 km s^{-1} to $+60$ km s^{-1} at 30 km s^{-1} intervals. We made our observations at the same velocities in each line of the [S II] doublet and Hα to obtain complete spatial maps of the [S II] $\lambda6716/\lambda6731$ and [S II] $(\lambda6716 + \lambda6731)$/Hα line ratios. The background below ~ 2 σ of the mean sky was excluded when ratioing images, to restrict the analysis to bright regions.

In addition to the Fabry-Perot data, we obtained low-dispersion long-slit spectra of the HH 46/47 system on the CTIO 4 m telescope in 1992 February using the R-C spectro-graph and Air Schmidt camera with Reticon CCD. The wavelength coverage was from 3500 Å to 3700 Å with spectral resolution $\delta\lambda = 11$ Å FWHM. We were careful to obtain the spectra of HH 46/47 when the jet axis was aligned roughly with the parallactic angle to minimize atmospheric refraction effects. The slit was positioned through the photocenter of HH 47A at a position angle of 57° and had a width of $\sim 2''6$. Although the sky was clear, the seeing was a mediocre $\sim 3''$. Three spectra with exposure times of 1200 s each were acquired, which were averaged to increase the signal-to-noise ratios and to eliminate cosmic-ray events using the **avsigclip** option in the IRAF **imcombine** routine. A He-Ne-Ar comparison source was used to wavelength-calibrate the spectra, and several spectrophotometric standard stars were observed through an 8″ slit to obtain reliable flux calibrations. We used standard IRAF reduction techniques to bias-subtract, flat-field, extract, sky-subtract, wavelength-calibrate, and flux-correct the spectra.

3. VELOCITY FIELD, ELECTRON DENSITIES, AND EXCITATION CONDITIONS

Figure 1 shows a contour plot of the [S II] and Hα emission of the HH 46/47 jet, where we have used the naming convention of RH91 to identify the main features of the outflow. Our Fabry-Perot observations provide detailed information from spatially resolved kinematic and line ratio maps over the entire flow region. Figures 2, 3, and 4 (Plates 32–33) show the heliocentric velocity field, the electron densities, and [S II]/Hα ratios, respectively, in HH 46/47.

The velocity field in Figure 2 was constructed from Gaussian fits to $\sim 10,000$ line profiles. We co-added the [S II] and Hα emission at each observed velocity to enhance the signal-to-noise ratios in faint regions. A high-velocity jet flows from the region of HH 46 near the IR source up to the working surface HH 47A. The jet appears to meander slightly along the flow, and the fastest material is confined to the axis while slower material is located at the edges of the jet (see Hartigan et al. 1993). The jet enters HH 47A slightly off-axis to the north where the ejected material is abruptly decelerated. Ahead of HH 47A is a bridge of faint emission that connects to the outer bow shock HH 47D. The light green area behind the apex of HH 47D envelopes the region that both HRM90 and RH91 have identified as the Mach disk of HH 47D, where the jet material is slowed. Note that the velocity fields in HH 47A and HH 47D are each consistent with that expected from a bow shock (see HRH87, HRM90): the highest velocities are found at the apex, and progressively lower velocities are found along the wings of the bow shocks.

Figure 3 maps electron densities throughout the HH 46/47 system, obtained from the [S II] $\lambda6716/\lambda6731$ ratio at each position over a range in velocities where HH 47A and HH 47D are brightest (~ -90 to -60 km s^{-1} heliocentric). The electron densities are highest at the base of the jet in HH 46. This situation is similar to that found in the "classical" jets, such as HH 34 and HH 111, though here the field is complicated by emission scattered from the surrounding reflection nebula. The electron densities are also very high in HH 47A. The spatial distribution is again that expected from a bow shock: the electron densities are highest at the apex, and fall off as the effective shock velocity decreases in the wings. Elsewhere, along the jet and in HH 47D, the signal-to-noise ratios are typically not high and the electron densities do not appear smoothly distributed. Nonetheless, it is evident that the electron densities in
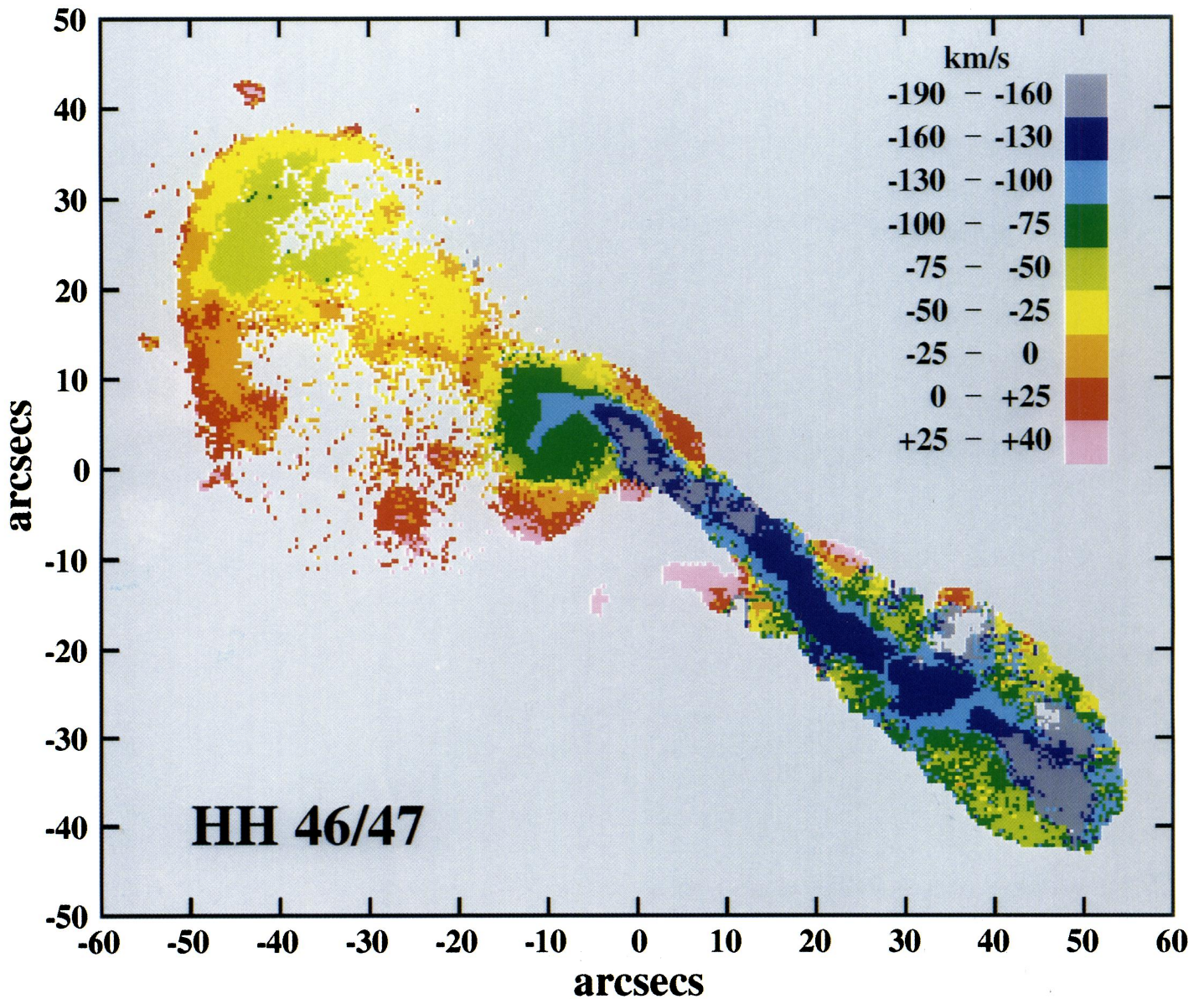
PLATE 32

FIG. 2.—Map of the velocity field of HH 46/47 based on Gaussian fits to the observed line profiles in the Fabry-Perot data (e.g., see the solid lines in Fig. 9). The heliocentric velocity ranges corresponding to each color are indicated. The systemic velocity of the ambient cloud emission is $\sim +25$ km s^{-1} (HRM90). The velocity fields in HH 47D and HH 47A are each consistent with a bow shock morphology: the highest blueshifted velocities are observed at the apices, and the radial velocities gradually decrease toward the bow shock wings (see HRH87).
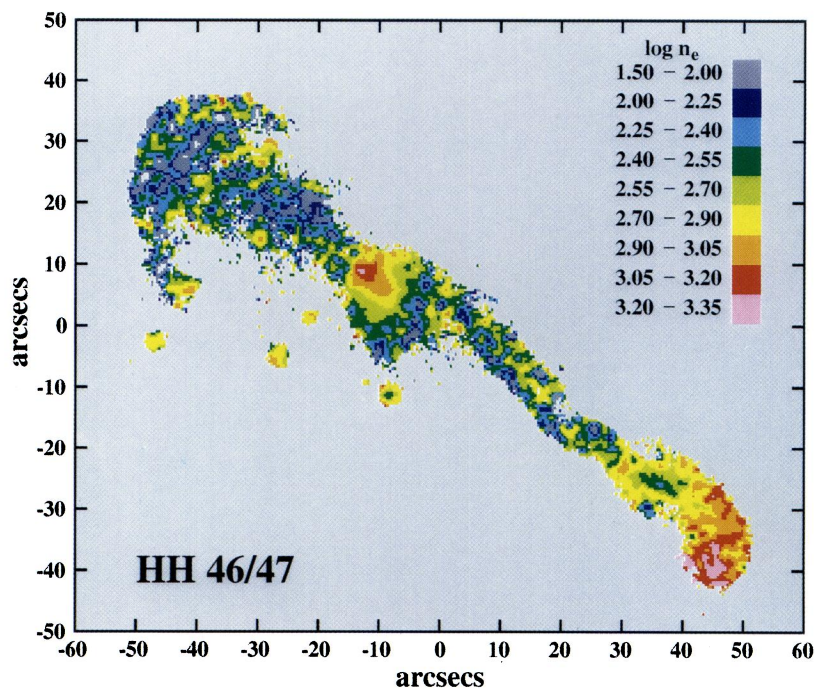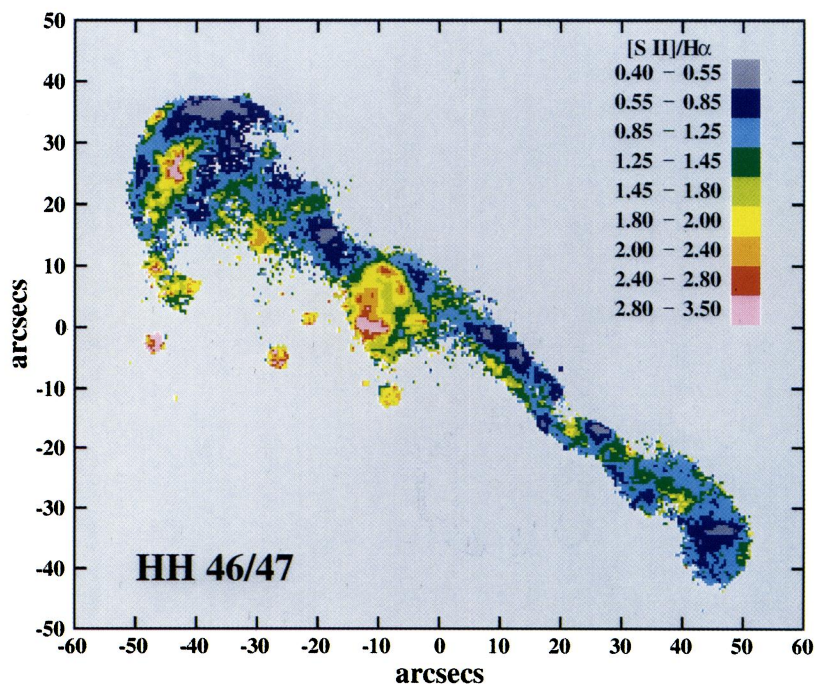
MORSE et al. (see 425, 740)

PLATE 33

FIG. 3

FIG. 4

FIG. 3.—Map of the electron densities obtained from the [S II] $\lambda\lambda6716/6731$ ratio for emisson in the heliocentric velocity range ~ -60 to -90 km s^{-1}, i.e., at velocities where emission from HH 47A and the outer bow shock HH 47D is strongest. Values of log n_e corresponding to each color are indicated. The two photon continuum emission arises from the position of greatest compression at the apex of the HH 47A bow shock.

FIG. 4.—Map of the [S II]/Hα ratios for emission at the same velocities as in Fig. 3. Values of [S II]/Hα corresponding to each color are indicated. The Mach disk in HH 47D identified by HRM90 and RH91 is visible as the region of very high [S II]/Hα values several arcseconds behind the edge of the bow shock toward the stellar source. The Mach disk in HH 47A, first seen by RH91, is located in the small region of relatively low [S II]/Hα values through the interior of the bow shock. The velocities sampled here do not cover the brightest emission from the Mach disk in HH 47A, however (see Fig. 2).

MORSE et al. (see 425, 740)

HH 47D are significantly lower than those in HH 47A. We should emphasize that the electron densities shown in Figure 3 (as well as the [S II]/Hα ratios in Fig. 4) are roughly monochromatic and may differ significantly from values obtained from the velocity-integrated [S II] line ratios measured in long-slit spectra (see the discussion in Morse et al. 1992). As previously noted, we chose velocities that highlight the spatial distribution of electron densities in the HH 47D and HH 47A bow shocks, but these do not sample the brightest emission from the higher velocity jet (see Fig. 2).

The [S II]/Hα ratios in Figure 4 show a wide range of gaseous excitation throughout the flow. At the base of the jet, HH 46 and most of the reflection nebula are brighter in Hα at the velocities sampled (same velocities as in Fig. 3). The Hα emission along the jet generally is stronger along the edges relative to [S II], which may denote locations where the jet entrains the surrounding material (see Hartigan et al. 1993). As first detailed by RH91, the HH 47A and HH 47D working surfaces each differ in gaseous excitation along the leading edges versus through the interior, but in the opposite sense: Hα generally dominates along the edges and [S II] dominates through the interior of HH 47D, while in HH 47A, a [S II]–bright region surrounds a planar-looking Hα bright feature in the interior. (Note that some of the [S II] bright spots are stars; see Fig. 1.)

4. SHOCK MODELS FOR HH 47D

4.1. *Bow Shock Velocity*

HRM90 modeled HH 47D as a 110 km s^{-1} bow shock viewed at an angle to the line of sight of $\phi \sim 45°$ which was moving into a fully preionized, stationary medium. They estimated the shock velocity and viewing angle by comparing the observed position-velocity diagram from long-slit spectra with theoretical position-velocity profiles generated from the bow shock models described by HRH87. The preshock medium was assumed to be fully ionized based on the brightness of the background emission from the Gum nebula. In addition, shock models in this range of shock velocities that assume full preionization agree much better with the strong [O II] λ3727 emission observed from HH 47D than do models assuming equilibrium preionization (e.g., see HRH87).

We are able to improve on the analysis of HRM90 by using our Fabry-Perot spectra and new radial-velocity and proper motion results from Heathcote & Reipurth (1994). We employ the following three arguments to estimate a bow shock velocity of ~70 km s^{-1} for HH 47D.

Bow shock kinematics.—When the cooling distance behind a spatially resolved bow shock is small compared to the size of the bow shock, we can approximate the emission as arising from a thin surface of revolution about the flow axis and use the formalism of HRH87 to estimate the bow shock velocity. The velocity field generated by the deflection of postshock material in this situation depends entirely on the geometry of the bow shock and the inclination of the flow axis toward the observer, with more blueshifted emission arising from the apex region and more redshifted emission from the bow shock wings. Comparing the distinctly "hook-shaped" high-resolution position-velocity diagrams observed by HRM90 and Heathcote & Reipurth (1994) with those predicted by the bow shock models of HRM90 suggests that HH 47D is a particularly good case to model. HRH87 found that for a radiative bow shock inclined at an angle ϕ to the line of sight

between 0° and 90°, the range in radial velocities produced by the deflection of postshock material is approximately equal to the shock velocity, V_S. From the velocity map in Figure 2, we estimate the velocities in HH 47D to range from ~ −110 km s^{-1} to ~ −40 km s^{-1} with respect to the ambient cloud emission (~ +25 km s^{-1}), thus indicating $V_S \approx 70$ km s^{-1}.

HRM90 derived a larger shock velocity of $V_S = 110$ km s^{-1} for HH 47D because they were unable to distinguish kinematically the emission in their Hα spectrograms arising in the extreme bow shock wings from the bright Gum nebula emission. They assumed that HH 47D was the primary ejection in the outflow and, thus, was moving into a stationary medium. In the bow shock models of HRH87, the radial velocity of the emisson from the extreme bow shock wings lies near (or is slightly redshifted from) the systemic radial velocity of the preshock medium *independent of the orientation of the bow shock to the line of sight.* Our Fabry-Perot images clearly distinguish the low-velocity emission from the extreme bow shock wings of HH 47D; this emission does *not* lie at the rest-frame velocity of the ambient cloud emission. We, therefore, conclude that HH 47D is *not* moving into a stationary medium.

Strong [O II] *λ3727 emission.*—HRM90 assumed the preshock medium of HH 47D was fully ionized because it is projected outside the host globule into the H II region ionized by the nearby O stars ζ Pup and γ^2 Vel. They also cited the overall agreement of the strong [O II] emission detected in their [O II] image with shock models assuming a fully preionized medium rather than equilibrium preionization (see HRH87). Figure 5 shows our long-slit spectrum of HH 47D extracted from the apex region. The observed line identifications and line ratios appear in Table 2. While the spectrum of this faint bow shock does not have a high signal-to-noise ratio, the strong [O II] λ3727 emission is evident. Comparing the observed [O II] λ3727/Hβ and [O II] λ3727/[O III] λ5007 line ratios with the fully preionized shock models in HRH87 (and Morse 1992), we find that shock velocities of ~60–70 km s^{-1} provide a much better agreement than do shock velocities of ≃ 100 km s^{-1}.

[O III] *λ5007 distributions.*—The bow shock velocity can be derived independently of the observed kinematics from the spatial distribution of [O III] λ5007 emission, similar to the method we employed in our study of the HH 34 bow shock (Morse et al. 1992). We constrained the shock velocity at the apex of HH 34 by measuring the bow shock shape, inclination angle, and assuming that with approximately equilibrium preionization conditions, [O III] λ5007 ceased to emit in the bow shock wings at a perpendicular shock velocity of ~100 km s^{-1}.

During the 1992 January run, we removed the etalon from the Fabry-Perot and acquired at 600 s image of HH 46/47 through an [O III] filter ($\lambda_{cen} = 4993$ Å; $\delta\lambda = 38$ Å FWHM). We detected [O III] λ5007 emission from the HH 47D bow shock and nowhere else in HH 46/47. The detection was confirmed in the long-slit spectrum of HH 47D (Fig. 5). Figure 6 overlays the faint [O III] emission with the emission summed over the [S II] data cubes. Although we may not be detecting faint [O III] emission in the bow shock wings, the emission is located along the leading edge at the apex of HH 47D and appears to cut off abruptly in the wings relative to the [S II] emission.

In the fully preionized models of HRH87 and Morse (1992), [O III] λ5007 ceases to emit strongly between shock velocities of ~60–50 km s^{-1}. Assuming that this is the perpendicular shock velocity at the point where the [O III] emission cuts off
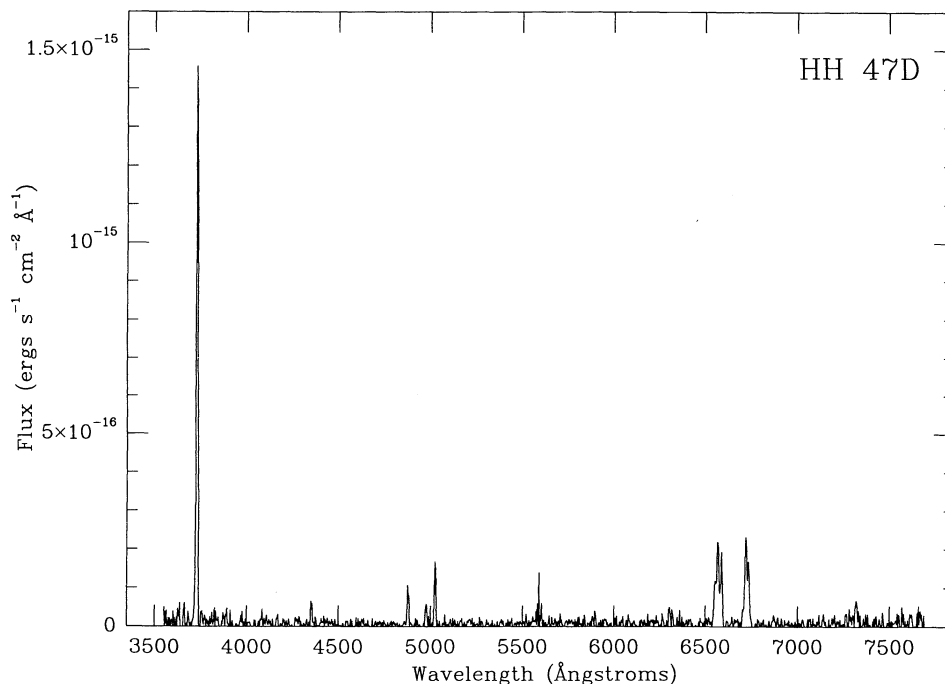
FIG. 5.—Flux-calibrated low-resolution spectrum of HH 47D, obtained with the R-C spectrograph on the CTIO 4 m telescope. The slit passed through the photocenter of HH 47A and the apex of HH 47D at a position angle of 57°, and had a width of 2″.6. Note the strong emission from [O II] $\lambda3727$ and the [O III] doublet at ~ 5000 Å. The emission line identifications and measured line ratios are given in Table 2.
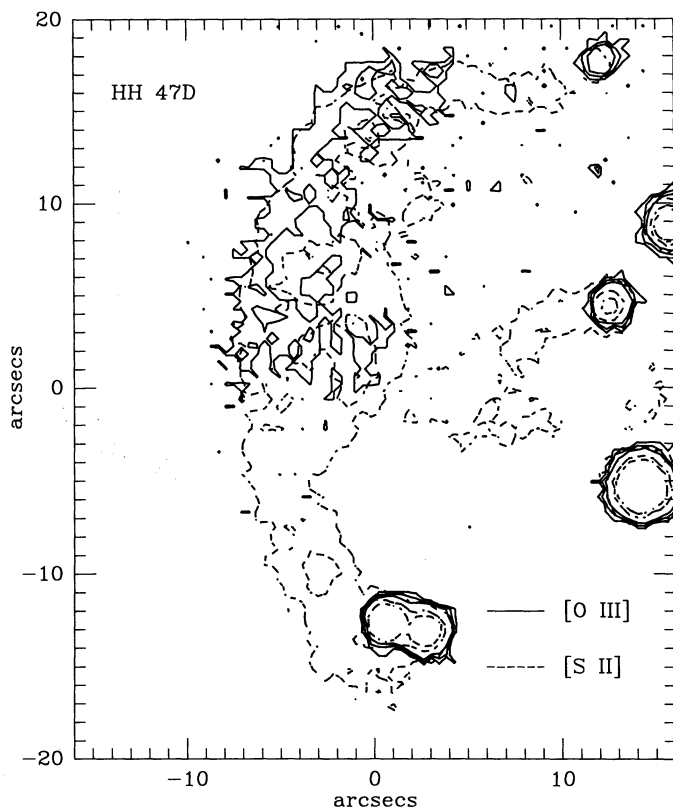

FIG. 6.—Contour plot overlaying the [O III] emission distribution with the [S II] emission in HH 47D. The images have been spatially registered to within 0″.2 using nearby stars as tie points. The [O III] emission is confined to a thin region at the apex of the bow shock which cuts off abruptly in the bow shock wings relative to the [S II] emission.

in the wings of HH 47D, we can apply equation (5) from Morse et al. (1992) to estimate the shock velocity at the apex of HH 47D. We adopt an inclination to our line of sight of $\sim 65°$ for the HH 46/47 system, as determined by Heathcote & Reipurth (1994) based on their new radial-velocity and proper-motion measurements. We also adopt the paraboloidal form for the true bow shock shape given in HRM90 (rescaled by the new inclination angle) of $Z = 0.0338R^2$, where Z is the distance from the apex along the flow axis corresponding to the radial distance R from the axis to the bow shock wing, both measured in arcseconds (see Fig. 1 of HRH87). Substituting these measurements into equation (5) of Morse et al. (1992) along with the values for the cutoff shock velocity $V_\perp = V_c \approx 55$ km s^{-1}, and a critical radius $2R_c \approx 21″ \pm 2″$ for the extent of [O III] emission, the predicted shock velocity at the apex of HH 47D is $V_S \approx 70 \pm 10$ km s^{-1}. The error accounts primarily for the uncertainties in V_c and R_c. Note that a viewing angle of $\phi \sim 55°$ (e.g., see Eislöffel & Mundt 1994) changes the calculated V_S by only a few km s^{-1}. Given the low surface brightness of HH 47D, the kinematic derivation of the shock velocity may be more reliable in this instance, but the agreement of the two methods is encouraging.

4.2. Preshock Density

We have calculated a grid of planar shock models as a basis for our bow shock model of HH 47D (see below). We estimated the preshock density, n_0, to be used in the calculations from the observed Hα flux at the apex of HH 47D summed over the region that emits [O III], where the shock velocities are reasonably well known. The observed Hα flux over this region is $F_{Hα} \approx 5.4 \times 10^{-14}$ ergs s^{-1} cm^{-2}. There may be a small contribution to this flux by the Mach disk because the [O III] emission overlaps slightly with the region that HRM90 and RH91 identify with the Mach disk of HH 47D. However, as

discussed below, Hα does not emit strongly from the Mach disk in HH 47D. We have corrected this Hα flux for reddening as follows: We measured the Hα/Hβ ratio in a spectrum of the preshock region immediately ahead of HH 47D extracted from our long-slit data. We assumed that this Gum nebula emission arises from material at nearly the same distance as the HH 46/47 system and estimated the differential reddening using the standard extinction law described in Cardelli, Clayton, & Mathis (1989) required to adjust the observed Hα/Hβ ratio to ~3, appropriate for case B recombination. The observed Hα/Hβ ≈ 3.5 ± 0.2 in the preshock spectrum indicates that $A_V = 0.57 \pm 0.17$ and $E(B-V) = 0.18 \pm 0.05$. The reddening corrected Hα flux at the apex of HH 47D is then 8.2×10^{-14} ergs s^{-1} cm^{-2}. Using equation (8) from Morse et al. (1992), with an effective shock velocity $V_{app} \approx 60$ km s^{-1}, a cross-sectional area of the emitting region $\sigma_c = \pi R_c^2 \approx 346$ arcsec$^2 \approx 1.6 \times 10^{34}$ cm^2, assuming a distance to HH 46/47 of 450 pc (RH91), and a value of $f_{H\alpha} \approx 0.42$ as the number of Hα photons produced per H atom crossing the shock, we derive a preshock density of $n_0 \approx 16 \pm 8$ cm^{-3}, where the error includes uncertainties in R_c, V_{ap}, $f_{H\alpha}$, the reddening correction and the Hα flux.

4.3. Planar Shock Models

We calculated planar shock models with the code described in Raymond (1979) and HRH87, using the updated atomic rates summarized in Cox & Raymond (1985). We generated models over a range in shock velocities from 30 to 80 km s^{-1} to account for the variation of the perpendicular shock velocity along the bow shock. Our calculations predict the total emission spectrum from a shock by following an element of gas as it passes through the shock, is heated and ionized, then radiatively cools and recombines.

We assumed a preshock temperature of 10^4 K in all the models, that H and He were singly ionized in the preshock gas, and set the elemental abundances to the cosmic values of Allen (1973); H = 12.0, He = 10.93, C = 8.52, N = 7.96, O = 8.82, Ne = 7.92, Mg = 7.42, Si = 7.52, S = 7.20, Ar = 6.80, Ca = 6.30, Fe = 7.60, and Ni = 6.30. We followed the methods of Raymond, Wallerstein, & Balick (1991) for including the ambient radiation field produced by early-type stars in the Gum nebula in the models. While this ambient radiation field can enhance the ionization of the preshock gas as well as the strengths of the Balmer lines and the forbidden lines of singly or doubly ionized species in the postshock recombination zone, we found very little difference in the predicted fluxes and line ratios compared to models that did not include the ambient field. This is because for reasonable distances to ζ Pup and γ² Vel, the stellar radiation can ionize the low density preshock gas, but it has little effect on the compressed postshock material. We assumed equal electron and ion temperatures throughout the flow. Calculation of the emission-line fluxes was terminated either when the gas temperature cooled below 1000 K or the cooling time exceeded 1000 yr, approximately the dynamical lifetime of HH 47D. We chose small step sizes to sample adequately the postshock temperatures near 10^4 K where the cooling gas becomes optically thick to Lyman-continuum photons.

Low signal-to-noise ratios in the [S II] data hamper our measurements of the postshock electron densities in HH 47D shown in Figure 3. Typical values along the leading edge of the apex are ~300 cm^{-3}. Given our estimated preshock density, there was better agreement between the observed and predict-

ed [S II] λ6716/λ6731 ratios using a preshock magnetic field $B_0 \sim 8$ μG than with no magnetic field. Table 1 shows the predicted emission line fluxes, normalized to the flux of Hβ = 100, from the planar shock models. The corresponding computed cooling times and distances are also indicated.

4.4. The Bow Shock Model

Table 2 lists our observed, reddening-corrected, and predicted optical line ratios in HH 47D. We note that some of the observed line ratios differ significantly from those reported by Dopita et al. (1982b), who measured strong emission from several low-excitation lines such as [N I] and [O I]. Also note that our observed line ratios may include some flux from the Mach disk (see below), though the slit was not placed over the brightest portion of this region. The theoretical line ratios were predicted for a 70 km s^{-1} bow shock, using the bow shock geometry described in HRH87. The bow shock was partitioned into a series of annuli, given a bow shock shape and shock velocity at the apex, as determined above. The flux from each annulus in the desired emission line is that produced by a planar shock of velocity $V_\perp$ weighted by the area of the annulus (see HRH87). The emission in each annulus was linearly interpolated between the fluxes given in Table 1 from the shock velocities bracketing $V_\perp$. We incorporated the effects of the finite slit width of 2″6 by summing the flux over the area in each annulus that is subtended by the slit, i.e., if the radius of the annulus was less than or equal to half the slit width, the entire flux from the annulus was used; otherwise, the flux was integrated over the area of the overlapping region. Seeing effects were not included; however, these should not be significant because the bow shock is much larger than the slit width. Because the extraction of the HH 47D spectrum was largely guided by the spatial extent of [O III] emission along the slit, the model line fluxes were integrated over annuli with shock velocities $V_\perp \geq 40$ km s^{-1}.

All of our predicted line ratios agree with the observed quantities to within 27%, roughly consistent with the measurement errors. We have achieved a very good agreement with the observed Balmer decrement and [O III] line strengths, and successfully reproduced a very large [O II] λ3727/Hβ ratio. The models underestimate the total [S II] flux and overestimate the [N II] flux, which may indicate deviations in the relative abundances from the solar values. But the overall match to the observed spectrum is quite remarkable given the simple bow shock model used in the calculations. The [N I] and [O I] emission calculated in our models is weak (see Table 1) because the preshock gas is ionized, in agreement with the lack of detected [N I] and [O I] emission in our spectrum of HH 47D. While the line ratios predicted by us and HRM90 derive from very similar planar shock models (except that we have tailored our shock input parameters to match the observed postshock fluxes and [S II] line ratios), there are two main reasons that we are able to achieve a better match to the observed line ratios than do HRM90. First, we used a bow shock velocity of 70 km s^{-1} instead of 110 km s^{-1}, which, as we have noted, provides a much better agreement to the observed [O II] λ3727/Hβ and [O III] λ5007/Hβ line ratios. Second, we have included the effects of an entrance slit in our predictions, while HRM90 integrated their line ratios over the whole bow shock. Integrating over the whole bow shock strongly biases the computed line ratios toward the fluxes generated in annuli at low shock velocities because of their large areas.

TABLE 1

PREDICTED EMISSION-LINE FLUXES IN HH 47D FROM PLANAR SHOCK MODELS WITH SOLAR ABUNDANCES

MODEL	D080	D070	D060	D050	D040	D030
V_S (km s^{-1})	80	70	60	50	40	30
X (H I)	0	0	0	0	0	0
Y_0 (He I)	0	0	0	0	0	0
Y_1 (He II)	1	1	1	1	1	1
n_0 (cm^{-3})	16	16	16	16	16	16
B_0 (μG)	8	8	8	8	8	8
T_{1000} (K)	4588	4340	2682	2085	2800	4058
d_{c4} (AU)	91	111	234	263	301	401
d_{c3} (AU)	768	795	815	849	907	1069
τ_{c4} (yr)	159	196	132	151	176	222
τ_{c3} (yr)	1000	1000	1000	1000	1000	1000
$F_{H\beta}$ [1]	.227	.193	.158	.124	.087	.052
He II 304	2400	882	170	10.4	0.1	0
C III 977	2380	1840	989	206	7.6	0.3
N III 991	199	158	76.9	10.5	0.5	0
S III 1198	260	259	203	78.1	6.2	0.6
Si III 1206	600	595	471	254	87.1	19.1
Ly α 1216	4034	4073	4127	4162	4141	3756
C II 1336	546	586	644	611	321	95.6
Si IV 1397[2]	272	191	99.0	35.9	7.5	0.7
O IV] 1402[3]	22.1	3.4	0.1	0	0	0
N IV] 1486	13.8	3.3	0.2	0	0	0
C IV 1549	280	56.4	3.8	0	0	0
He II 1640	7.5	1.9	0.2	0	0	0
O III] 1663[2]	256	210	78.2	5.3	0.1	0
N III] 1750[3]	96.7	86.9	55.0	12.0	1.0	0.1
Si III] 1891	327	350	333	254	149	71.8
C III] 1908	950	858	616	224	19.8	2.2
N II] 2141[2]	23.0	25.3	31.2	35.9	24.9	13.1
C II] 2326[3]	400	427	470	504	411	259
Si II] 2340[3]	10.9	11.8	12.5	12.9	12.5	11.2
[Ne IV] 2423[2]	2.7	0.2	0	0	0	0
[O II] 2470	38.1	43.4	61.2	60.5	41.5	26.4
Mg II 2799[2]	74.7	75.0	75.9	108	262	539
Mg I 2852	5.2	4.4	5.1	5.7	8.7	25.4
[O II] 3726	468	512	664	699	582	490
[O II] 3729	584	662	893	960	809	693
[Ne III] 3869	57.7	40.8	9.7	0.5	0	0
Ca II 3945[2]	28.1	23.3	18.9	20.3	25.3	40.8
[Ne III] 3968	18.3	13.0	3.1	0.1	0	0
[S II] 4072[2]	18.2	17.7	17.4	19.3	23.3	22.8
Ca I 4227	4.9	3.7	1.7	1.5	1.8	2.6
[O III] 4363	41.4	35.6	14.5	1.1	0	0
[Fe III] 4658	19.5	21.3	23.6	27.2	27.8	24.3
Hβ 4861	100	100	100	100	100	100
[O III] 4959	165	149	67.9	6.3	0.1	0
[O III] 5007	481	434	198	18.5	0.3	0
[N I] 5200[2]	19.6	16.2	12.0	13.2	16.9	26.7
[N II] 5755	5.9	6.4	7.5	8.8	7.5	5.4
He I 5876	14.8	14.1	13.5	13.4	13.2	13.1
[O I] 6300	41.4	31.4	18.2	17.8	21.8	28.4
[O I] 6363	13.8	10.5	6.1	5.9	7.3	9.5
[N II] 6548	65.9	64.9	63.6	71.5	74.2	76.8
Hα 6563	302	303	310	313	309	298
[N II] 6583	195	192	188	212	220	227
He I 6678	4.4	4.2	4.0	3.9	3.9	3.8
[S II] 6716	186	173	148	160	205	241
[S II] 6731	150	137	116	122	152	174
[Ca II] 7306[2]	9.8	7.7	5.1	5.0	5.9	8.5
[O II] 7320	28.2	32.1	45.3	44.8	30.7	19.5
[O II] 7331	22.7	25.8	36.4	36.0	24.7	15.7
[Fe II] 8617	2.5	2.2	1.8	1.9	2.3	3.0
[C I] 8727	1.6	1.4	1.3	1.5	1.8	2.0
[S III] 9069	14.6	13.8	11.8	9.2	2.9	1.5
[S III] 9532	38.0	35.8	30.6	23.9	7.5	4.0
[C I] 9823	16.2	14.2	11.6	12.2	14.0	15.2
[C I] 9850	47.9	41.9	34.5	36.1	41.5	45.1

TABLE 1—*Continued*

MODEL	D080	D070	D060	D050	D040	D030
[S II]10289,339[2]	6.4	6.2	6.1	6.8	8.2	8.0
[S II]10323,373[2]	5.8	5.6	5.6	6.2	7.5	7.3
[N I]10402[2]	0.7	0.6	0.5	0.6	0.7	1.2
He I 10830	19.4	18.2	16.5	15.8	16.2	17.2
[Ne II] 12.8μ	52.7	48.8	40.4	36.3	26.5	16.3
[Ne III] 15.6μ	34.1	25.1	6.4	0.4	0	0
[Si II] 35.3μ	431	415	391	372	364	361
[O I] 63.2μ	58.5	50.5	37.8	32.0	31.3	29.7
2 photon	329	351	382	416	412	227

Note.—All fluxes are normalized to $H\beta = 100$. The parameters X, Y_0, and Y_1 refer to the ionization state of the preshock gas; n_0 is the preshock density; B_0 is the preshock magnetic field strength; d_{c4} and d_{c3} are the distances between the shock and the position where the postshock temperature $T = 10^4$ K and $T = 10^3$ K, respectively, while τ_{c4} and τ_{c3} are the corresponding cooling times; T_{1000} refers to the postshock temperature reached when calculation of the emission-line fluxes was terminated, which was limited to a maximum cooling time of 1000 yr.

[1] Flux of $H\beta$ in units of 10^{-4} ergs s^{-1} cm^{-2} through *front* of shock.

[2] Line is a doublet.

[3] The ^4P–^2P intersystem transitions consist of five closely spaced lines (Mendoza 1983). There are seven lines of O iv] and Si iv] between 1393 Å and 1407 Å.

4.5. *Kinematics of the Preshock Medium: Evidence for Prior Ejections?*

To estimate the outward velocity of the preshock medium, we matched the velocity field of our bow shock model to the observed velocity field of HH 47D (Fig. 2; see also Fig. 2 of Hartigan et al. 1993). The bow shock model was calculated relative to a restframe radial velocity of 0 km s^{-1}, and we found good correspondence if we shifted the model by $\sim -50 \pm 15$ km s^{-1}. This corresponds to a shift from the systemic velocity of the ambient cloud emission (at $\sim +25$ km s^{-1}) of $\sim -75 \pm 15$ km s^{-1}, implying that the preshock medium of HH 47D has an outward velocity of $V_{\text{med}} \sim 180 \pm 35$ km s^{-1} with respect to the exciting star for a viewing angle of $\phi \sim 65°$. Combined with our estimated shock velocity of $V_S \approx 70$ km s^{-1}, we predict a space velocity of $V_{\text{space}} \sim 250$ km s^{-1} and a tangential velocity of $V_{\text{tan}} \sim 230$ km s^{-1}. We emphasize that while the values we derive for V_{med}, V_{space}, and V_{tan} may change somewhat if, for instance, a different viewing angle is chosen, the $\sim 20\%$ uncertainties in the numbers do not alter the overall picture that the effective shock velocity at the apex of HH 47D is much smaller than the space velocity. It is

TABLE 2

Observed[a] (F), Reddening-corrected[b] (F_0), and Model[c] Line Ratios in HH 47D

Line	F	F_0	MODEL
[O ii] $\lambda\lambda3726, 3729$	1513	1832	1484
$H\beta$ $\lambda4861$	100	100	100
[O iii] $\lambda4959$	54	53	51
[O iii] $\lambda5007$	158	154	148
$H\alpha$ $\lambda6563$	374	313	310
[N ii] $\lambda6583$	177	148	203
[S ii] $\lambda6716$	251	208	168
[S ii] $\lambda6731$	173	143	129

[a] Measurement uncertainties are typically $\pm 20\%$ for unblended lines and somewhat worse for blended or poorly sky-subtracted lines.

[b] Corrected according to a standard extinction law with $E(B - V) = 0.18$.

[c] Predictions for bow shock velocity at apex ≈ 70 km s^{-1} and slit width of $2\farcs6$ positioned along the axis of symmetry. Seeing effects are ignored.

therefore likely that HH 47D is not the first ejection in the system but follows in the wake of previously ejected material, as was the case for the most prominent blueshifted bow shocks in the HH 34 and HH 111 stellar jet systems (Morse et al. 1992, 1993a).

We have looked for evidence of an ejection prior to HH 47D by imaging through a 12 Å FWHM $H\alpha$ filter. Figure 7 (Plate 34) shows the average of two deep 1500 s images obtained with the CTIO 4 m telescope on 1993 February 8 of the region $\sim 2'$ ahead of HH 47D. We clearly detect a diffuse emission feature $\sim 50''$ ahead of HH 47D, similar to the separation between HH 47D and HH 47A. This feature can also be seen in the deep $H\alpha$ image of Olberg et al. (1992). Unfortunately, our Fabry-Perot images did not cover this region, and because of its off-axis location, our long-slit spectrum also missed the structure, so we have no kinematic or line ratio information about the emission. However, if this structure represents shocked material from an outflow event prior to HH 47D that was either deflected away from the current jet axis or was ejected along a slightly different direction than subsequent ejections, we predict that the emission should have a radial velocity of approximately $-V_{\text{med}} \cos \phi \sim -75$ km s^{-1} relative to the exciting star. In the absence of kinematic data we must be cautious about regarding this feature as part of the HH 46/47 outflow since there are several such filamentary emission-line structures along the edges of the 210-6A globule.

4.6. *The Mach Disk of HH 47D*

The Mach disk of HH 47D that has been identified by HRM90 and RH91 is well defined in our Fabry-Perot data. It is most visible in Figure 4 as the region of high [S ii]/$H\alpha$ ratios several arcseconds toward the stellar source from the edge of the bow shock. Both HRM90 and RH91 recognized the low excitation of the central knot in this region and inferred that such a spectrum would be expected from the jet shock if the jet material was denser than the ambient medium. Our data show that this region has extremely low electron densities (Fig. 3), indicating a weak shock, as well as the highest radial velocity in HH 47D (Fig. 2), arising from the inclination of the system off the plane of the sky. We also observed these characteristics in the Mach disk of HH 34 (Morse et al. 1992).

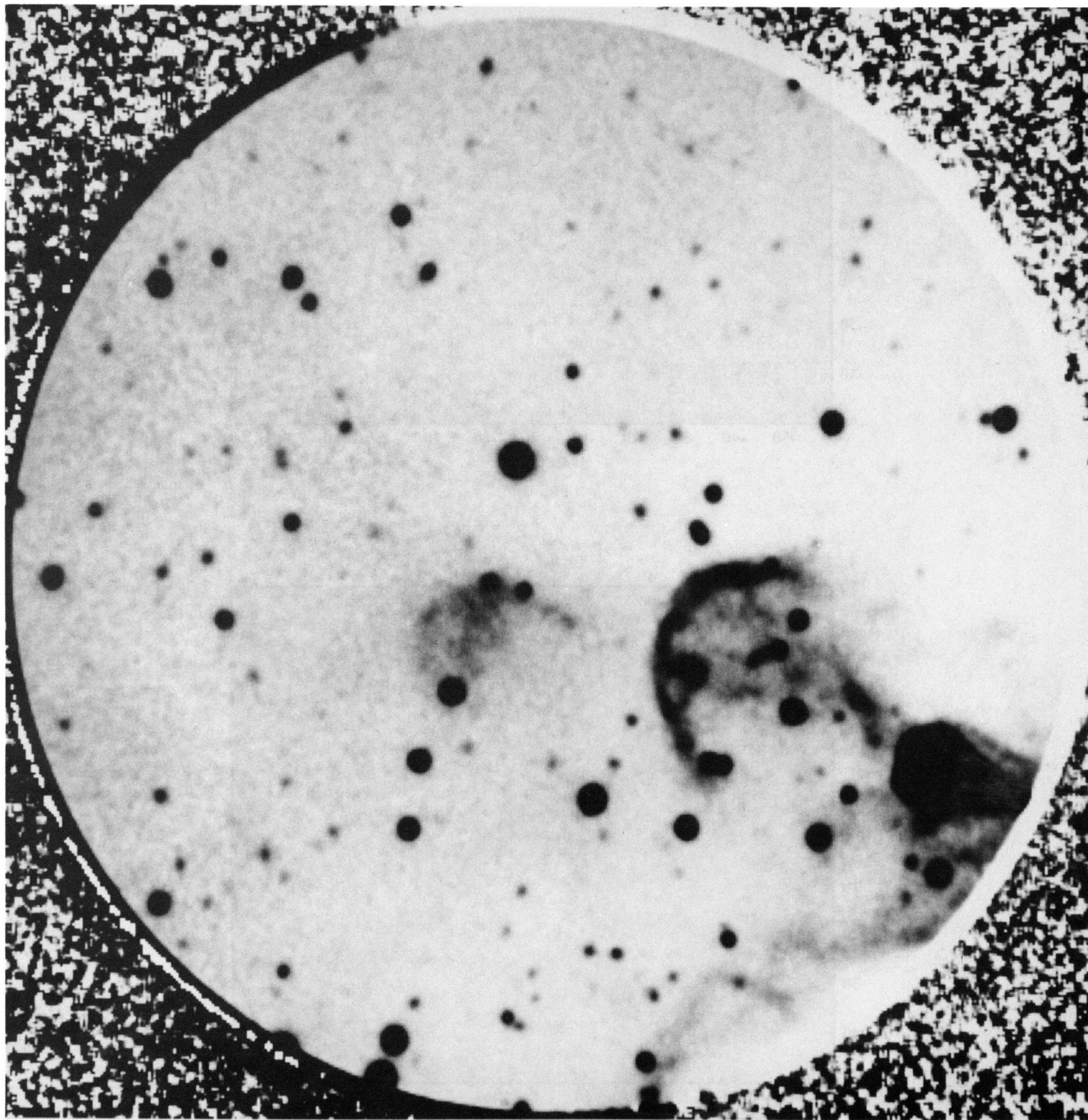The high [S ii]/$H\alpha$ ratios in the Mach disk indicate that the

Fig. 7.—Average of two deep Hα images of the HH 47D preshock region taken in mediocre seeing on the CTIO 4 m telescope through the Fabry-Perot with the etalon removed. The circular field of view is ~2.5 in diameter. We detect a diffuse, off-axis emission feature ~50″ ahead of HH 47D in the center of the field which may come from material ejected prior to HH 47D.

Morse et al. (see 425, 745)

shock velocity is probably ~20–30 km s^{-1}. Assuming that this is the case, by balancing the ram pressures in the Mach disk and bow shock—using equation (11) in Morse et al. (1992) with $n_0 = 16$ cm^{-3}, $V_{BS} = 70$ km s^{-1}, $V_{MD} = 25$ km s^{-1}, and $\beta \approx 1$—we estimate a jet density of $n_j \sim 125$ cm^{-3}, and therefore a jet-to-ambient density ratio $n_j/n_0 = \eta \approx 8$. There are large uncertainties in the values for n_j and n; however, it is clear that the Mach disk is a much weaker shock than the bow shock, and, therefore, the jet material is significantly denser than the ambient medium.

5. SHOCK MODELS FOR HH 47A

5.1. Bow Shock Velocity and Preshock Density

The low-resolution spectra that we extracted for the other regions in the blueshifted lobe of the HH 46/47 system are shown in Figure 8. The regions are labeled according to the designations given in Figure 4 of RH91. These spectra, which are strongly dominated by low-excitation line species (e.g., [O I], [N I], [S II], [Ca II], and [Fe II]), are qualitatively different from the spectrum of HH 47D (Fig. 5), which is dominated by higher ionization species (e.g., [O II], [O III], and [N II]). The measured line ratios for most of the major emission

lines are given in Table 3. We corrected the line ratios for interstellar extinction using the correction we applied to HH 47D. However, the reddening may increase toward the regions closer to the stellar source because the emission emanates from deeper within the host globule. In fact the stellar source is completely obscured at optical wavelengths by intervening material. We also note that the prevalence of Fe lines and higher overall ratios of metal lines to H as compared to the line ratios measured in the HH 34 and HH 111 systems (see Morse et al. 1993b) suggests that the abundances in HH 46/47 are not depleted as in Orion (e.g., see Osterbrock, Tran, & Veilleux 1992) but are more nearly solar.

HRM90 modeled HH 47A as a ~110 km s^{-1} bow shock moving into a preshock medium with an outward velocity of ~90 km s^{-1}. This scenario was invoked to explain the kinematics of HH 47A implied in the position-velocity profile. A bow shock model moving into a stationary preshock medium could not explain their HH 47A observations because the systemic radial velocity tail in the position-velocity profile was blueshifted from the rest velocity of the parent globule. However, our new data suggest that the bow shock velocity must be somewhat lower than HRM90 preferred. HRM90 based their estimate on the measured Hα line width in HH

TABLE 3

OBSERVED[a] (F) AND REDDENING-CORRECTED[b] (F_0) LINE RATIOS IN HH 46/47

Line	HH 47A		A$_9$ – A$_{26}$		HH 47B		B$_3$ – B$_{11}$		HH 46 + RN	
	F	F_0	F	F_0	F	F_0	F	F_0	F	F_0
[O II] λλ3726, 3729 ..	97	117	163	197	—	—	75	91	29	35
Ca II λ3933	56	66	19	22	188	221	100	118	66	78
Ca II λ3968, Hε λ3970	48	56	22	26	101	118	54	63	33	39
[S II] λλ4069, 4076 ..	78	90	15	17	152	175	91	105	133	153
Hδ λ4102	20	23	20	23	15	17	10	11	14	16
[Fe II] λ4244	14	16	4	5	42	47	22	25	35	39
[Fe II] λλ4277, 4287 .	23	26	9	10	74	82	33	37	44	49
Hγ λ4341	40	44	43	47	32	35	30	33	32	35
[Fe II] λ4358	14	15	7	8	44	48	21	23	35	38
[Fe II] λ4415	20	22	8	9	48	52	28	30	41	44
Mg I λ4571 [c]	44	46	15	16	115	121	49	52	19	20
[Fe II] λ4815	9	9	2	2	19	19	10	10	20	20
Hβ λ4861	100	100	100	100	100	100	100	100	100	100
[Fe II] λ5112	5	5	—	—	13	13	7	7	20	19
[Fe II] λ5159	40	38	10	10	98	94	50	48	78	75
[N I] λλ5198, 5201 ...	138	131	44	42	426	405	194	185	55	52
[Fe II] λλ5262, 5272 .	23	22	—	—	61	58	34	32	93	88
[Fe II] λ5334	6	6	—	—	14	13	9	8	36	34
[Fe II] λ5527	5	5	—	—	—	—	7	6	26	24
[O I] λλ6300, 6364 ...	465	397	173	148	1368	1169	713	609	687	587
Hα λ6563	472	395	425	356	766	642	590	494	878	735
[N II] λ6583	66	55	78	65	44	37	126	105	113	95
[S II] λ6716	515	426	173	143	1308	1082	642	531	202	167
[S II] λ6731	413	341	120	99	902	746	453	374	201	166
[Fe II] λ7155	34	27	5	4	68	54	45	36	142	113
[Fe II] λ7172	5	4	—	—	14	11	8	6	34	27
[Ca II] λ7291	131	104	28	22	312	247	133	105	107	85
[Ca II],[O II] λ7325 [d]	91	72	29	23	218	172	101	80	142	112
[Ni II] λ7379 [e]	35	27	—	—	—	—	29	23	93	73
[Fe II] λ7452	10	8	—	—	—	—	17	13	46	36

[a] Measurement uncertainties are typically ±10% for strong, unblended lines, and ~ ±20% for weak, blended, or poorly sky-subtracted lines.
[b] Corrected according to a standard extinction law with $E(B-V) = 0.18$.
[c] Blend with [Mg I] λ4562 and several Fe II lines.
[d] Blend of [Ca II] λ7324 and [O II] λλ7319, 7330.
[e] Ambiguous identification.

HH 47A

FIG. 8a

HH 47 jet, $A_9 - A_{26}$
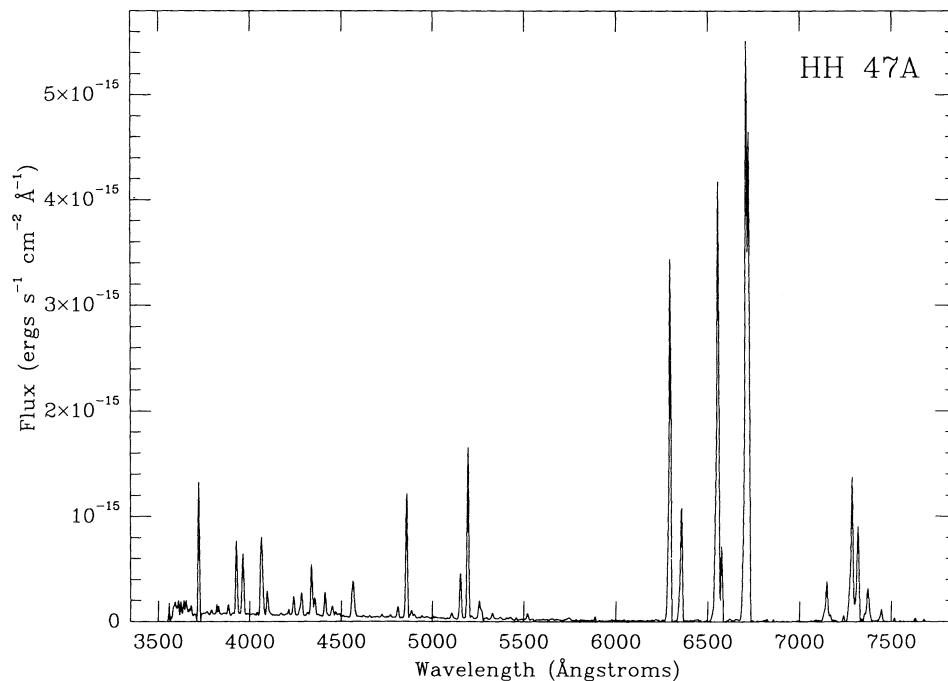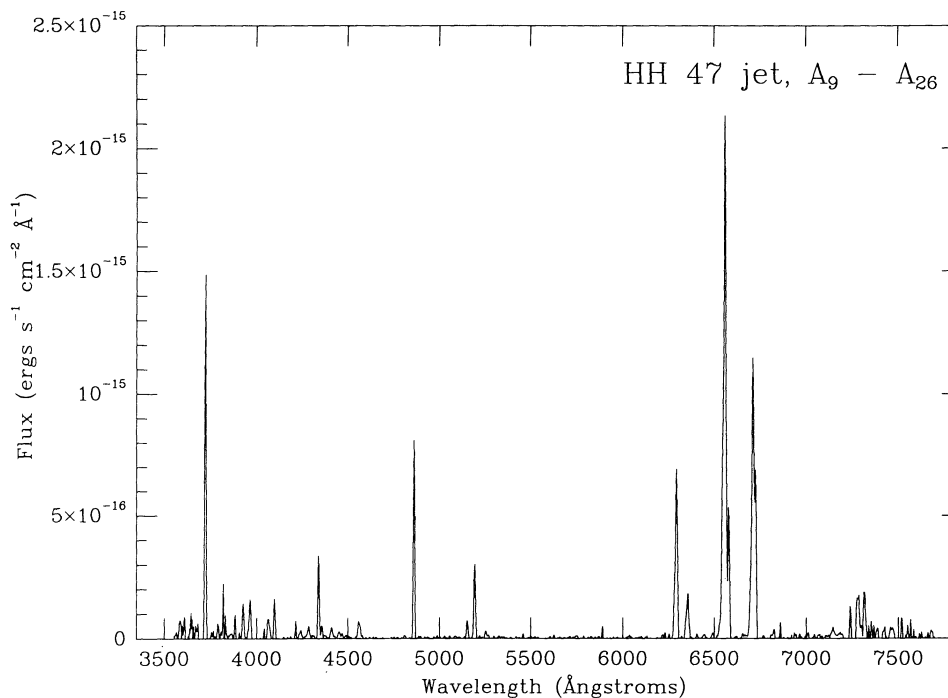
FIG. 8b

FIG. 8.—Flux-calibrated low-resolution spectra of the various regions along the HH 46/47 jet, obtained in the same manner as in Fig. 5. The spectra are labeled using the designations given in RH91. The spectra have been summed over regions along the slit that included (a) HH 47A, (b) the jet knots A_9 through A_{26}, (c) HH 47B, (d) the jet knots B_3 through B_{11}, and (e) HH 46 plus reflection nebula. The measured line ratios from the major emission lines identified in the spectra are given in Table 3. The blue continuum in the HH 47A spectrum is due to two-photon emission at the apex of the bow shock, while the red continuum in the spectrum of HH 46 arises from scattered light from the obscured stellar source.
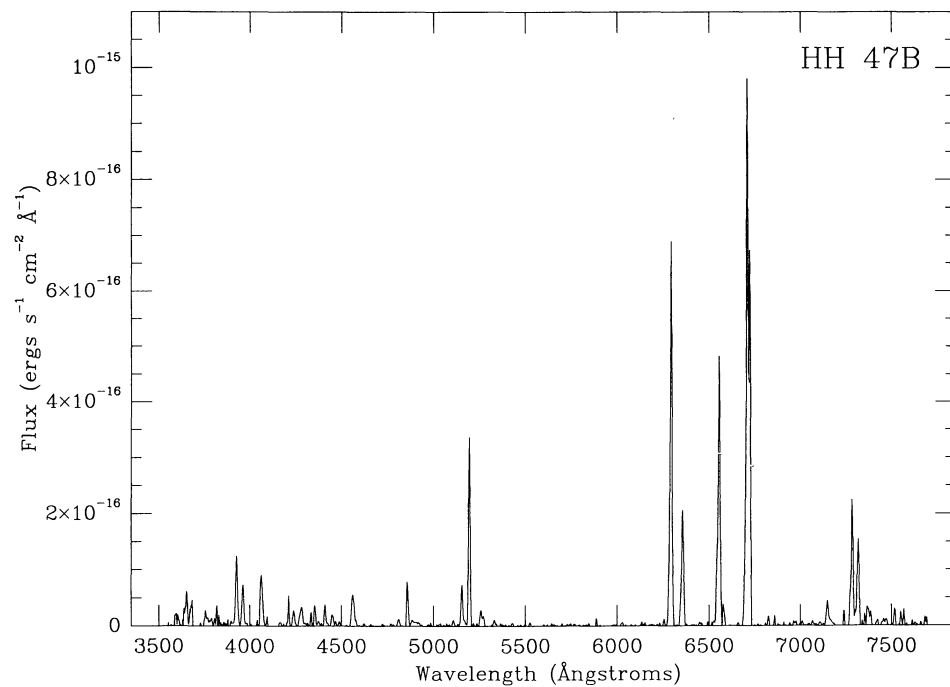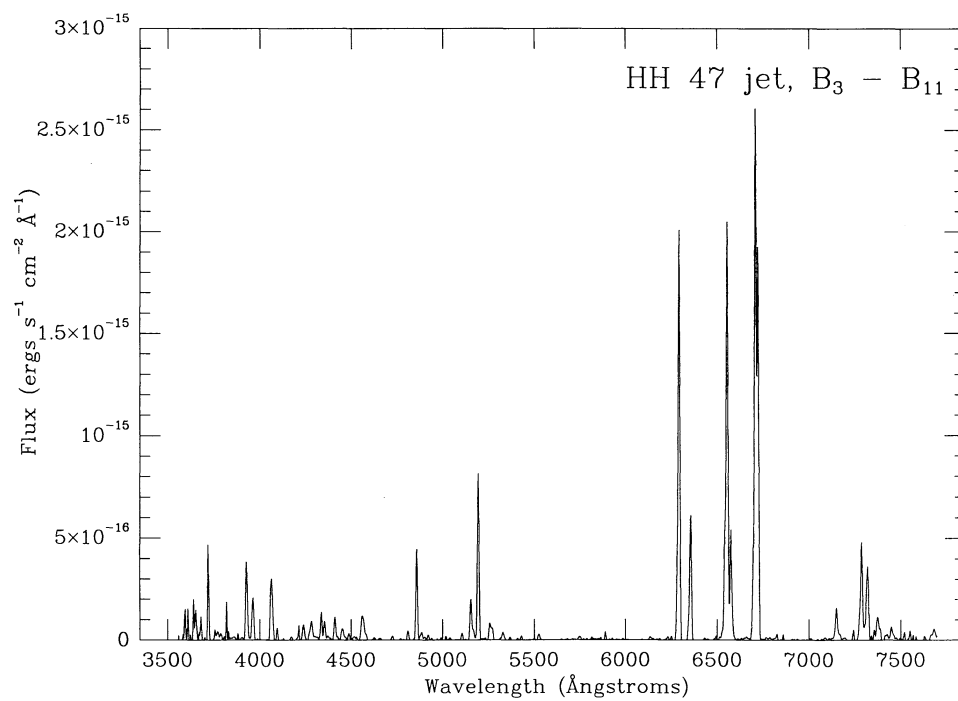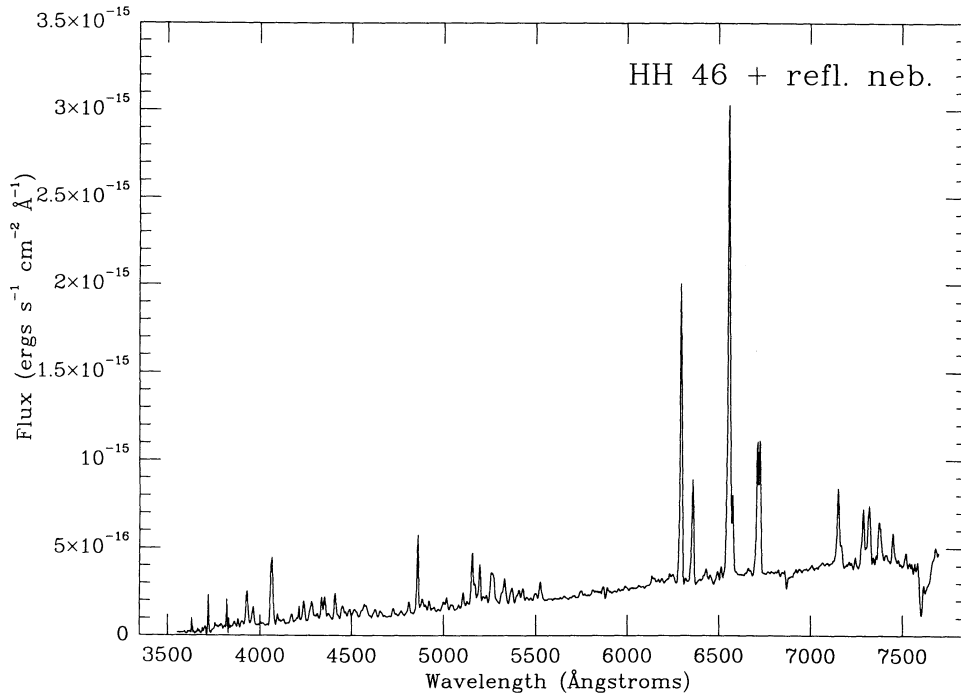
HH 47B

FIG. 8c

HH 47 jet, $B_3 - B_{11}$

FIG. 8d

FIG. 8e

47A, but we have seen, e.g., in HH 34 and HH 111V (Morse et al. 1992, 1993a), that the Hα line width may not be a good indicator of the shock velocity when line-broadening mechanisms other than the postshock deflection of material become important. If a significant fraction of neutral H crosses the shock, then much of the Hα flux will be collisionally excited in the very hot region immediately behind the shock. The line width will then reflect the temperature of this hot zone ($\sim 10^5$ K for an 80 km s^{-1} shock; see Raymond 1979 and the discussion in Raga & Binette 1991) rather than the temperature in the recombination zone ($\sim 10^4$ K). In addition, as we discuss below, it is now clear that emission from the Mach disk is responsible for a large fraction of the Hα flux from HH 47A (RH91). The velocity dispersion in the Mach disk may be large compared to the bow shock if the incident jet material has a lower density than the ambient medium (Hartigan 1989). The most reliable evidence that the shock velocities in HH 47A are < 100 km s^{-1} is that [O III] emission is not detected in HH 47A, nor anywhere between HH 47A and the stellar source. As discussed in Morse et al. (1992, 1993a) and HRH87, even if the gas incident into the bow shock (or Mach disk) is completely neutral, the absence of [O III] emission implies a shock velocity < 100 km s^{-1} (see Fig. 5 in Morse et al. 1993a).

It is difficult to estimate the bow shock velocity for HH 47A from Figure 2 because there is no guarantee that the faint emission ahead of HH 47A lies in the path of the bow shock. The emission in the region between HH 47A and HH 47D may come from jet material that HH 47A is overtaking, or compressed ambient gas that has passed through the outer bow shock. The kinematics are consistent with the emission arising in the *foreground* bow shock wing of HH 47D, especially given the very extended wings in the [O II] image of HRM90.

The distribution of electron densities along the edges of HH 47A in Figure 3 show the exact morphology expected from a bow shock, with the highest values occurring at the apex and a gradual decrease in the postshock densities toward the bow shock wings. Such a morphology results from decreases in both the postshock compression and ionization fraction as the perpendicular shock velocity decreases from the apex to the bow shock wings. The electron densities in the postshock gas at the apex of the bow shock approach ~ 2000 cm^{-3}, about twice those in the Mach disk (see below). The [S II]/Hα ratios in Figure 4 along the edges of the bow shock also generally follow the expected distribution. The lowest values, showing where the hottest gas is located (for these relatively low shock velocities), are found at the apex and the values steadily increase into the wings, especially in the southern wing where very high values are found. The [S II]/Hα ratios of ~ 3–4 in the southern wing of the bow shock indicate shock velocities of probably $\lesssim 30$ km s^{-1} in this region (see HRH87). Overall, the [S II]/Hα ratios are much higher than those found in other high-velocity bow shocks such as HH 34, implying that the shock velocity is much lower than the velocity dispersion or the radial velocities would indicate. In addition, Dopita et al. (1982a) detected a blue continuum in HH 47A which they attributed to 2 photon emission from collisionally excited H. The 2 photon continuum can be seen in our spectrum of HH 47A (Fig. 8a). It was also detected in all of the low-velocity Fabry-Perot images that did not contain line emission from HH 47A, as well as in the narrow-band [O III] image. The 2 photon emission arises from a compact region in HH 47A that coincides with the region of highest electron densities in Figure 3, i.e., it comes exclusively from the apex of the bow shock and *not* from the Mach disk. The presence of 2 photon emission implies that collisional excitation of H is important at the apex of the bow shock and, therefore, that the preshock medium *must* contain a significant neutral fraction.

RH91 showed that the outer edges of HH 47A are dominated by [S II] emission, while there is a linear, Hα-bright feature perpendicular to the jet axis nestled in the interior

which they identified as the Mach disk in HH 47A. Our Fabry-Perot observations strongly support this identification (see also Hartigan et al. 1993). In Figure 2, this linear feature is kinematically associated with the head of the jet and is distinct from the bow shock. In Figure 4, the higher excitation nature of this feature is evident, although the velocities sampled in this illustration do not include the maximum intensity from the Mach disk. For this reason the [S II]/Hα ratios in Figure 4 appear higher in the Mach disk than those reported in RH91. In the high-velocity image ratios, the Mach disk has [S II]/Hα values typically ~0.7, while in Figure 4 the Mach disk emission is much fainter at the velocities sampled and overlaps with emission from the [S II]–bright foreground (and possibly background) bow shock wing.

Based on the observed excitation state in the postshock gas in HH 47A and the presence of 2 photon emission at the apex of the bow shock, we conclude that (1) the shock velocity in the Mach disk is higher than at the apex of the bow shock; (2) the shock velocities are <100 km s^{-1}; and (3) collisional excitation is important in both shocks. Because the first conclusion suggests that the density of the incident jet material is lower than the density in the material ahead of HH 47A (possibly the wake of HH 47D), we infer that most of the Hα line broadening in HH 47A is generated by the Mach disk.

The low excitation of the bow shock emission, especially in the wings, and the presence of 2 photon emission indicates that the bow shock velocity is quite low, perhaps ~50–60 km s^{-1} at the apex. Using this estimate, we calculated the preshock density, n_0, from the Hα flux observed at the apex of the bow shock, carefully omitting emission from the Mach disk. Using equation (8) from Morse et al. (1992)—with the following parameters: $V_{ap} \sim 50$ km s^{-1}, $F_{H\alpha} \sim 1.3 \times 10^{-13}$ ergs s^{-1} cm^{-2} (corrected for reddening), $\sigma_c \sim 21.2$ arcsec$^2 \approx 9.63 \times 10^{32}$ cm^{-2} at a distance of $d = 450$ pc (RH91), and $f_{H\alpha} \approx 0.21$—we find $n_0 \approx 1020 \pm 400$ cm^{-3}, where the uncertainties are primarily in $f_{H\alpha}$, $F_{H\alpha}$, and V_{ap}. While the uncertainty in our estimate of the preshock density is large, the value we derive is consistent with the observation that the HH 47A bow shock is very bright but has a low excitation.

5.2. *Planar Shock Models*

We calculated planar shock models for the HH 47A bow shock, which we tabulate in Table 4. Given the presence of 2 photon emission, we assumed equilibrium preionization conditions in our planar shock models for HH 47A (see HRH87), which for these shock velocities amounts to assuming that the incident gas is neutral. This is in contrast to the situation for HH 47D, which appears to have propagated beyond the confines of the parent cloud into the ionized medium of the Gum nebula (§ 4.1). Given our estimates for the bow shock velocity and preshock density, we then found a preshock magnetic field strength of $B_0 \sim 140$ μG was necessary to restrict the postshock [S II] $\lambda6716/\lambda6731$ ratios to the observed values. Our shock models in Table 4 can be compared to similar models presented in HRH87 that do not include magnetic fields and have [S II] ratios close to the high density limit. We note that Hodapp (1987) found evidence from near-infrared polarimetry that the magnetic field in the vicinity of HH 47A is aligned perpendicular to the jet axis, and would therefore be important in inhibiting the compression across the bow shock. Although we have included a sizable magnetic field in the planar shock models, in general the cooling times are short and the cooling distances less than 1" at the distance of HH 46/47.

5.3. *The Bow Shock Model*

We constructed a model of the HH 47A bow shock using the planar shock models in Table 4. In Figure 9 we compare grids of the observed (*solid lines*) and predicted (*dotted lines*) Hα line profiles across HH 47A. The individual line profiles have been summed over 2 × 2 pixels, or 0".8 × 0".8 bins. We assumed a bow shock velocity of $V_S \approx 60$ km s^{-1}, a bow shock shape of $Z \approx 0.2R^2$, where Z and R are measured in arcseconds (see HRH87 and HRM90), and an inclination to the line of sight of $\phi \sim 65°$. The theoretical monochromatic Hα images were smoothed spatially by a Gaussian seeing profile of 1".3 FWHM and in velocity by a thermal broadening of 80,000 K, corresponding to the temperature in the postshock region near the apex where Hα is collisionally excited.

Figure 9 shows that the Hα velocity field and line fluxes are well matched by the bow shock model throughout most of the apex region. It also delineates the Mach disk behind the apex of the bow shock (above 0" along the vertical axis) where the observed line profiles have a strong blueshifted emission component not reproduced by the model. The model line profiles needed to be blueshifted in radial velocity by $\sim -120 \pm 15$ km s^{-1} (relative to the systemic radial velocity of the globule $\sim +25$ km s^{-1}) to align with the observed profiles. For a viewing angle of $\phi \sim 65°$, this implies an outward velocity for the preshock medium of $\sim 285 \pm 35$ km s^{-1}, and a space velocity of ~ 345 km s^{-1} for the HH 47A working surface. We should note that the quality of the match between the observed and predicted line profiles through much of the bow shock in Figure 9 is in part due to the smoothing effect of the seeing conditions. Images obtained in subarcsecond seeing (e.g., RH91; Eislöffel & Mundt 1994) show that the bow shock emission is very clumpy on small scales which would not be well matched by a uniform bow shock model.

5.4. *The Mach Disk in HH 47A*

Figure 2 may provide the first quantitative estimate of the shock velocity in the Mach disk of a Herbig-Haro object. The jet material just before HH 47A enters with a radial velocity of ~ -180 km s^{-1} relative to the exciting star, while the Mach disk emission has a radial velocity of ~ -140 km s^{-1}. This velocity difference corresponds to a shock velocity at the Mach disk of ~ 95 km s^{-1} when a viewing angle of $\phi \sim 65°$ is taken into account, which is only just below the limit imposed by the absence of observable [O III] emission (§ 5.1). We must be cautious, however, because the jet appears to enter the working surface off-center and the Mach disk emission may have a significant velocity component perpendicular to the jet axis which would affect the observed radial velocity. In fact, in the simple steady state working surface model, the Mach disk should have roughly the same radial velocity as the apex of the bow shock. The difference in HH 47A is ~ 15 km s^{-1}, which may indicate either nonsteady conditions, or possibly significant "side-splash" of the post-Mach disk jet material. Substituting our tentative preshock density and shock velocities for the HH 47A bow shock and Mach disk into equation (11) of Morse et al. (1992) yields a jet-to-ambient density ratio of $\eta \sim 0.6$.

5.5. *Molecular Emission in HH 47A*

The velocity of the HH 47A preshock medium fits in nicely with our estimated space velocity for the previous ejection HH 47D, but it raises interesting questions about the nature of the

TABLE 4

PREDICTED EMISSION-LINE FLUXES IN THE HH 47A BOW SHOCK FROM PLANAR SHOCK MODELS
WITH SOLAR ABUNDANCES

MODEL	A060	A050	A040	A030
V_S (km s^{-1})	60	50	40	30
X (H I)	.99	1	1	1
Y_0 (He I)	1	1	1	1
Y_1 (He II)	0	0	0	0
n_0 (cm^{-3})	1020	1020	1020	1020
B_0 (μG)	140	140	140	140
T_{1000} (K)	1000	1000	1000	1164
d_{c4} (AU)	1.1	2.7	8.8	56
d_{c3} (AU)	131	194	412	1471
τ_{c4} (yr)	0.7	1.7	5.3	31
τ_{c3} (yr)	95	138	289	1000
$F_{H\beta}$ [1]	7.19	3.28	1.13	.232
C III 977	0.4	0.3	0.1	0
S III 1198	0.3	1.0	0.4	0.1
Si III 1206	0.2	0.1	0	0
Ly α 1216	7300	8502	11145	18532
C II 1336	10.5	14.0	24.1	57.2
Si III] 1891	0.2	0.1	0	0
C III] 1908	1.4	1.1	0.3	0
N II] 2141[2]	1.1	1.7	1.4	0 6
C II] 2326[3]	27.4	42.9	88.2	290
Si II] 2340[3]	2.9	4.6	9.2	30.1
[O II] 2470	1.7	1.0	0.6	0.3
Mg II 2799[2]	62.5	47.7	185	814
Mg I 2852	2.3	2.0	8.5	62.6
[O II] 3726	26.9	21.8	15.5	10.6
[O II] 3729	17.2	18.8	18.2	15.1
Ca II 3945[2]	7.5	11.6	30.7	251
[S II] 4072[2]	8.6	8.2	17.2	52.4
Ca I 4227	0.8	1.1	2.2	10.5
Hβ 4861	100	100	100	100
[N I] 5200[2]	7.3	18.2	69.1	293
[N II] 5755	0.7	0.9	0.7	0.3
He I 5876	0.4	0.2	0.1	0.2
[O I] 6300	41.6	75.8	165	551
[O I] 6363	13.9	25.3	55.0	184
[N II] 6548	14.3	18.0	13.1	6.0
Hα 6563	334	360	415	531
[N II] 6583	42.4	53.1	38.6	17.9
He I 6678	0.2	0.1	0.1	0
[S II] 6716	38.4	66.3	214	817
[S II] 6731	54.1	73.0	179	577
[Ca II] 7306[2]	2.8	4.3	9.6	56.3
[O II] 7320	1.3	0.8	0.4	0.2
[O II] 7331	1.0	0.6	0.3	0.2
[Fe II] 8617	1.7	2.7	5.6	18.6
[C I] 8727	1.1	1.4	2.4	4.7
[S III] 9069	2.0	7.8	4.2	0.9
[S III] 9532	5.3	20.2	10.8	2.3
[C I] 9823	14.1	19.5	31.8	53.0
[C I] 9850	41.7	57.7	94.2	157
[S II]10289,339[2]	3.0	2.9	6.0	18.4
[S II]10323,373[2]	2.7	2.6	5.5	16.7
[N I]10402[2]	1.0	1.3	2.4	10.4
He I 10830	0.6	0.4	0.2	0.2
[Ne II] 12.8μ	24.7	56.1	83.8	64.8
[Ne III] 15.6μ	0.1	0.1	0	0
[Si II] 35.3μ	199	436	1230	4360
[O I] 63.2μ	51.6	93.1	221	1060
2 photon	1558	2199	3656	7772

NOTE.—All fluxes are normalized to Hβ = 100. The parameters X, Y_0, and Y_1 refer to the ionization state of the preshock gas; n_0 is the preshock density; B_0 is the preshock magnetic field strength; d_{c4} and d_{c3} are the distances between the shock and the position where the postshock temperature $T = 10^4$ K and $T = 10^3$ K, respectively, while τ_{c4} and τ_{c3} are the corresponding cooling times; T_{1000} refers to the postshock temperature reached when calculation of the emission-line fluxes was terminated, which was limited to a maximum cooling time of 1000 yr.

[1] Flux of Hβ in units of 10^{-4} ergs s^{-1} cm^{-2} through *front* of shock.

[2] Line is a doublet.

[3] The ^4P–^2P intersystem transitions consist of five closely spaced lines (Mendoza 1983). There are seven lines of O IV] and Si IV] between 1393 Å and 1407 Å.
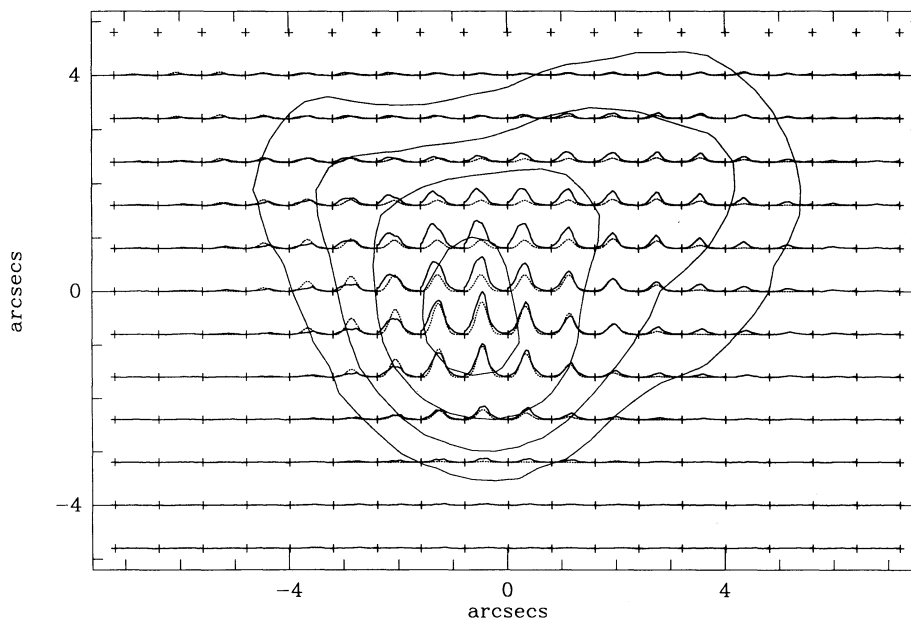
FIG. 9.—A comparison of the observed (*solid lines*) and predicted (*dotted lines*) Hα velocity fields in HH 47A. The HH 47A data have been rotated to align the jet axis approximately along the vertical axis, with the direction to the stellar source toward the top. The bow shock model used a bow shock velocity of 60 km s^{-1} observed at a viewing angle of $\phi \sim 65°$. The spectra are summed over 2 × 2 pixel bins and are normalized in the plot to the maximum of the highest peak to preserve the relative intensities as a function of position. The (heliocentric) velocity limits in each spectrum are from -210 km s^{-1} to $+30$ km s^{-1} and are sampled at 15 km s^{-1} intervals. The line profiles are well matched in the region near the apex of the bow shock. Note the strong blueshifted emission from the Mach disk $\sim 4''$ behind the apex.

molecular component of the HH 46/47 outflow. Various authors have recently suggested that the fast, collimated outflows seen as optical jets and HH objects might drive the more massive, poorly collimated, slower outflows observed in CO by entrainment (e.g., Chernin & Masson 1993; Raga & Cabrit 1993; Raga et al. 1993; Stahler 1993). Our Fabry-Perot observations of the HH 47 jet clearly show that entrainment occurs (Hartigan et al. 1993), though our observations pertain only to atomic material. Schwartz (1983) and Böhm, Scott, & Solf (1991) report H$_2$ emission bands in *IUE* spectra of HH 47A, and Wilking et al. (1990) detect the H$_2$ 1–0 $S(1)$ line at 2.12 μm. More recently, Zealey, Suters, & Randall (1993) have obtained H$_2$ images of HH 46/47 that show bright emission coincident with the reflection nebula near the source, along the edges of a cavity surrounding the obscured redshifted counterjet, and from the apex and northern wing of the HH 47A bow shock.

Molecular hydrogen emission is fairly common among HH objects, and its appearance in HH 47A, along with 2 photon emission, would not seem remarkable if the HH 47A preshock medium were ambient cloud material. However, the molecular emission at the apex of HH 47A means that (1) the 285 km s^{-1} preshock medium, which we know contains a significant fraction of neutral H by the presence of 2 photon emission, may also have a significant molecular component. This gas may have passed through a series of relatively weak bow shocks to acquire a high velocity without completely dissociating H$_2$; *or* (2) the postshock gas has cooled sufficiently for molecules to reform (see Hollenbach & McKee 1989), perhaps in a dense shell between the bow shock and Mach disk (e.g., see Blondin, König, & Fryxel 1989; de Gouveia Dal Pino & Benz 1993). In either case, it appears that the molecular material, which is not observed out beyond HH 47A, has been shielded from the

ionizing radiation of the Gum nebula which, according to Chernin & Masson (1991), destroys the CO beyond the edges of the cloud.

The molecular emission observed along the northern wing of HH 47A coincides with the low velocity emission shown in deep red in the velocity map of Figure 2. This region also has strong Hα emission (Fig. 4; see also Fig. 4 of Hartigan et al. 1993). While it is difficult to differentiate, this emission distribution appears to follow the model described by Raga & Cabrit (1993), where the extreme wing of the HH 47A bow shock is entraining low velocity molecular material, rather than entrainment by the high velocity jet. The low-velocity Hα emission in our Fabry-Perot data is connected to the rest of the bow shock (see the lower left panel of Fig. 2 in Hartigan et al. 1993). There does not appear to be an association between the molecular hydrogen emission and the entrainment of atomic gas occurring along the *blueshifted* jet in HH 46/47, nor is there clear evidence that the blueshifted jet is itself molecular.

The presence of molecular hydrogen emission from the apex of HH 47A may affect our estimate of the jet-to-preshock density ratio in that region. Our value of $\eta \sim 0.6$ (§ 5.4) rests on the shock velocities we have estimated for the HH 47A bow shock and Mach disk. However, the energy lost to molecular cooling behind a shock reduces the effective shock temperature for a given shock velocity, so that the optical emission spectrum resembles that of a somewhat slower shock (McKee & Hollenbach 1980; Curiel & Raymond 1993). If the gas ahead of HH 47A is fully molecular, the true bow shock velocity may be as high as ~ 75 km s^{-1}, rather than the 50–60 km s^{-1} we estimated based on the optical line ratios and line profiles. This higher shock velocity would result in a revised jet-to-preshock density ratio of $\eta \sim 0.8$.

6. SUMMARY AND CONCLUSIONS

We have obtained spectrophotometry of the stellar jet system HH 46/47 with an imaging Fabry-Perot spectrometer. Gaussian fits to ~10,000 spectral line profiles in the Fabry-Perot data produce a detailed map of the kinematics of the jet and working surfaces HH 47A and HH 47D. Monochromatic images of the [S II] $\lambda6716/\lambda6731$ and [S II] $(\lambda6716 + \lambda6731)$/H$\alpha$ line ratios yield maps of postshock electron densities and gaseous excitation throughout the entire flow.

We also present low-resolution spectra of the various flow regions along the jet, from HH 46 near the stellar source through the outer bow shock HH 47D. The measured emission line ratios indicate that the outer bow shock HH 47D has a higher excitation spectrum than the rest of the outflow, which we attribute to its location outside of the parent globule in the H II region ionized by nearby early-type stars.

A bow shock model for HH 47D has been constructed using the geometry described in Hartigan et al. (1987) and a new grid of planar shock models. Comparing the observed and predicted velocity fields and emission-line ratios leads us to the following conclusions about the HH 47D working surface:

1. The bow shock velocity is only ~70 km s^{-1}. We based our estimate on the velocity dispersion in the bow shock, the relative [O II] $\lambda3723$/Hβ and [O III] $\lambda5007$/Hβ line ratios, and the spatial distribution of the [O III] $\lambda5007$ emission.

2. By aligning the velocity field predicted by our bow shock model with the observed one, we estimated that the preshock medium has an outward velocity of ~180 km s^{-1}. Combining this with our estimated shock velocity, we derived a space velocity of ~250 km s^{-1} for HH 47D. As with the outer bow shocks in the HH 34 and HH 111 stellar jets, the bow shock velocity is much lower than the space velocity. We thus infer that HH 47D is not the primary ejection in this outflow but follows in the wake of previously ejected material. We observed some evidence for material ejected prior to HH 47D in a deep Hα image of the preshock region, but this identification awaits kinematic confirmation.

3. We have spatially and kinematically isolated the Mach disk in HH 47D, first identified by Hartigan et al. (1990). Its low excitation spectrum implies that the jet material is ~10 times denser than the preshock medium.

The working surface HH 47A has also been analyzed in detail, with the following results:

1. The absence of [O III] $\lambda5007$ emission indicates that the shocks in HH 47A have shock velocities less than 100 km s^{-1}.

2. The Mach disk first identified by Reipurth & Heathcote (1991) has been spatially and kinematically distinguished from the bow shock emission. The Mach disk is a linear feature aligned perpendicular to the flow axis and is kinematically associated with the jet material that enters the working surface. The Mach disk emission is of higher excitation than the bow shock emission, implying that it is a stronger shock and, therefore, that the jet material entering HH 47A has a lower density ($\eta \sim 0.6$) than the medium ahead of HH 47A. We also believe the large linewidths observed in HH 47A are generated pri-

TABLE 5
PROPERTIES OF BOW SHOCKS IN HH JETS

Parameter	HH 47D	HH 47A	HH 34	HH 111V
V_S (km s^{-1})	70	60	140	95
n_0 (cm^{-3})	16	1020	65	200
B_0 (μG)	8	140	15	30
V_{med} (km s^{-1})	180	285	150	305
$n_j/n_0 = \eta$	8	0.6	12	10

marily in the Mach disk since the velocity dispersion in the Mach disk of an underdense jet will be large (Hartigan 1989).

3. Based on the very low excitation optical emission in the bow shock and the presence of 2 photon emission from the apex region, we estimated a shock velocity at the apex of HH 47A of ~60 km s^{-1}. We compared the observed Hα line profiles to those predicted by a bow shock model and found kinematic evidence that the preshock medium has an outward velocity of ~285 km s^{-1}, similar to the space velocity for the previous ejection HH 47D. The presence of molecular hydrogen emission observed in HH 47A (Zealey et al. 1993) may indicate a somewhat higher bow shock velocity than we have estimated, and therefore a slightly slower preshock medium and denser jet material entering the Mach disk. The molecular hydrogen emission in the region appears to be associated with the HH 47A bow shock and not the high velocity jet.

Table 5 summarizes the shock parameters we derive for the two major bow shocks in the HH 46/47 outflow along with those we found for the brightest bow shocks in the HH 34 and HH 111 stellar jets (Morse et al. 1992, 1993a). For a distance to HH 46/47 of 450 pc, the kinematic age of HH 47D is ~1150 yr, based on the space velocity we determined of ~250 km s^{-1} assuming a viewing angle of ~65°. Similarly, with our estimated space velocity of ~345 km s^{-1} the kinematic age of HH 47A is ~550 yr, about half that of HH 47D. These estimates are uncertain because they assume the bow shocks have maintained a constant velocity (and flow direction), but they imply that the stellar source may undergo eruptive mass loss events every few hundred years. A similar dynamical timescale separating major bow shocks along stellar jets has been estimated in HH 34 (~400 yr; Reipurth & Heathcote 1992) and HH 111 (also ~400 yr; Reipurth et al. 1992). As Dopita (1978) suggested more than a decade ago, the HH 46/47 stellar jet may be driven by repetitive eruptions in the stellar energy source akin to FU Orionis–type outbursts that occur every several hundred years.

REFERENCES

Allen, C. W. 1973, Astrophysical Quantities (3d ed; London: Althlone)
Blondin, J. M., Königl, A., & Fryxell, B. A. 1989, ApJ, 337, L37
Böhm, K.-H., Scott, D. M., & Solf, J. 1991, ApJ, 371, 248
Bührke, T., Mundt, R., & Ray, T. P. 1988, A&A, 200, 99
Cardelli, J. A., Clayton, G. C., & Mathis, J. S. 1989, ApJ, 345, 245
Chernin, L. M., & Masson, C. R. 1991, ApJ, 382, L93

Chernin, L. M., & Masson, C. R. 1993, preprint
Cox, D. P., & Raymond, J. C. 1985, ApJ, 298, 651
Curiel, S., & Raymond, J. C. 1993, ApJ, submitted
Dopita, M. A. 1978, ApJS, 37, 117
Dopita, M. A., Binette, L., & Schwartz, R. D. 1982a, ApJ, 261, 183
Dopita, M. A., Schwartz, R. D., & Evans, I. 1982b, ApJ, 263, L73
Eislöffel, J. & Mundt, R. 1994, A&A, in press
Emerson, J. P., et al. 1984, ApJ, 278, L49
de Gouveia Dal Pino, E. M., & Benz, W. 1993, ApJ, 410, 686
Graham, J. A. 1987, PASP, 99, 1174
Graham, J. A., & Elias, J. H. 1983, ApJ, 272, 615
Graham, J. A., & Heyer, M. 1989, PASP, 101, 573
Hartigan, P. 1989, ApJ, 339, 987
Hartigan, P., Morse, J. A., Heathcote, S., & Cecil, G. 1993, ApJ, 414, L121
Hartigan, P., Raymond, J. C., & Hartmann, L. 1987, ApJ, 316, 323 (HRH87)
Hartigan, P., Raymond, J. C., & Meaburn, J. 1990, ApJ, 362, 624 (HRM90)
Hartley, M., Manchester, R. N., Smith, R. M., Triton, S. B., & Gross, W. M. 1986, A&A, 63, 27
Heathcote, S. R., & Reipurth, B. 1994, in preparation
Hodapp, K.-W. 1987, ApJ, 319, 842
Hollenbach, D., & McKee, C. F. 1989, ApJ, 342, 306
McKee, C. F., & Hollenbach, D. 1980, ARA&A, 18, 219
Meaburn, J., & Dyson, J. E. 1987, MNRAS, 225, 863
Mendoza, C. 1983, in IAU Symp. 103, Planetary Nebulae, ed. D. R. Flower (Dordrecht: Reidel), 143
Morse, J. A. 1992, Ph.D. thesis, Univ. of North Carolina
Morse, J. A., Hartigan, P., Cecil, G., Raymond, J. C., & Heathcote, S. 1992, ApJ, 399, 231
Morse, J. A., Heathcote, S., Cecil, G., Hartigan, P., & Raymond, J. C. 1993a, ApJ, 410, 764
Morse, J. A., Heathcote, S., Hartigan, P., & Cecil, G. 1993b, AJ, 106, 1139
Olberg, M., Reipurth, B., & Booth, R. S. 1992, A&A, 259, 252
Osterbrock, D. E., Tran, H. D., & Veilleux, S. 1992, ApJ, 389, 305
Pudritz, R. E., Pelletier, G., & Gomez de Castro, A. I. 1991, in The Physics of Star Formation and Early Stellar Evolution, ed. C. J. Lada & N. D. Kylafis (Dordrecht: Kluwer), 539
Raga, A. C., & Binette, L. 1991, Rev. Mexicana Astron. Af., 22, 265
Raga, A. C., & Cabrit, S. 1993, A&A, in press
Raga, A. C., Cantó, J., Calvet, N., Rodríguez, L. F., & Torrelles, J. M. 1993, A&A, 276, 539
Raga, A. C., & Mateo, M. 1987, AJ, 94, 684
Raymond, J. C. 1979, ApJS, 39, 1
Raymond, J. C., Wallerstein, G., & Balick, B. 1991, ApJ, 383, 226
Reipurth, B., & Heathcote, S. R. 1991, A&A, 246, 511 (RH91)
———. 1992, A&A, 257, 693
Reipurth, B., Raga, A. C., & Heathcote, S. 1992, ApJ, 392, 145
Schwartz, R. D. 1977, ApJ, 212, L25
———. 1983, ApJ, 268, L37
Schwartz, R. D., Jones, B. F., & Sirk, M. 1984, AJ, 1735
Stahler, S. 1993, in Astrophysical Jets, ed. M. Livio, C. O'Dea, & D. Burgarella (Cambridge: Cambridge Univ. Press), in press
Wardle, M., & Königl, A. 1993, ApJ, 410, 218
Wilking, B. A., Schwartz, R. D., Mundy, L. G., & Schultz, A. B. 1990, AJ, 99, 344
Zealey, W. J., Suters, M. G., & Randall, P. R. 1993, Proc. Astron. Soc. Australia, in press